DEPARTMENT OF PHYSICS
COLLEGE OF SCIENCES
OLD DOMINION UNIVERSITY
NORFOLK, VIRGINIA 23529

HYPERTHERMAL ATOMIC OXYGEN GENERATOR

By

Govind S. Khandelwal, Principal Investigator

and

Dongchuan Wu, Graduate Research Assistant

Final Report
For the period ended August 17, 1990

Prepared for
National Aeronautics and Space Administration
Langley Research Center
Hampton, Virginia 23665

Under
Research Grant NAG-1-1020
Dr. Ronald A. Outlaw
SSD-High Energy Science Branch

August 1990

Old Dominion University Research Foundation is a not-for-profit corporation closely affiliated with Old Dominion University and serves as the University's fiscal and administrative agent for sponsored programs.

Any questions or comments concerning the material contained in this report should be addressed to:

Executive Director
Old Dominion University Research Foundation
P. O. Box 6369
Norfolk, Virginia 23508-0369

Telephone: (804) 683-4293
Fax Number: (804) 683-5290

DEPARTMENT OF PHYSICS
COLLEGE OF SCIENCES
OLD DOMINION UNIVERSITY
NORFOLK, VIRGINIA 23529

HYPERTHERMAL ATOMIC OXYGEN GENERATOR

By

Govind S. Khandelwal, Principal Investigator

and

Dongchuan Wu, Graduate Research Assistant

Final Report
For the period ended August 17, 1990

Prepared for
National Aeronautics and Space Administration
Langley Research Center
Hampton, Virginia 23665

Under
Research Grant NAG-1-1020
Dr. Ronald A. Outlaw
SSD-High Energy Science Branch

Submitted by
Old Dominion University Research Foundation
P.O. Box 6369
Norfolk, Virginia 23508-0369

August 1990

FINAL REPORT NAG-1-1020

HYPERTHERMAL ATOMIC OXYGEN GENERATOR

The grant period of 15 months has primarily been used for further characterization of the transport properties of oxygen through silver. Specifically, experiments measuring the transport through Ag (111), Ag (110), Ag (100) single crystals and through Ag 0.05 Zr alloy were completed. In addition, experiments using glow discharge excitation of oxygen to assist in the transport have been completed. It was found that the permeability through the different orientations of single crystal Ag was the same, but significant differences existed in the diffusivity. The experimental ratio of diffusivities, however, was in reasonable agreement with theoretical estimates. Since the solubilities of orientations must be the same, this suggests some problems with the assumption K = DS. The glow discharge experiments show that there is a substantial increase in transport (factor of six) when the upstream pressure is dissociated to some fraction of atoms (which have a much higher sticking coefficient). These results indicate that there is a significant surface limitation because of dissociative adsorption of the molecules.

Experiments with the Ag 0.05 Zr alloy and its high-grain boundary and defect density show a permeability of greater than a factor of two over ordinary polycrystalline Ag, but it is unclear as to whether this is because of enhanced transport through these defects or whether the Zr and defects on the surface

increased the sticking coefficient and therefore the transport. Details of this work can be found in the attached Master's thesis by D. Wu.

APPENDIX

ABSTRACT

THE STUDY OF OXYGEN TRANSPORT THROUGH POLYCRYSTALLINE, SINGLE CRYSTAL AND ALLOYED SILVER

Dongchuan Wu

Old Dominion University, 1990

Director: Dr. G. S. Khandelwal and Dr. R. A. Outlaw

The permeation of oxygen through large grain polycrystalline silver, through the (110), (111) and (100) single crystals of silver and through Ag0.05Zr alloy have been studied over the temperature range of 400 - 800 °C. In addition, studies were also conducted using glow discharge dissociation of the supply side (upstream) molecular oxygen in order to examine whether normal dissociative adsorption is a limiting step in the overall transport process.

The permeability of oxygen through polycrystalline silver was found to be quite linear and quite repeatable. The diffusivity measurements were found to exhibit two distinct linear regions, one above and one below a critical temperature of 630 °C. The high-temperature data have an activation energy (11.1 kcal/mole) similar to that reported by others, but the low-temperature data have a comparatively larger activation energy (15.3 kcal/mole) which is probably due to the higher efficiency of traps.

The permeability of oxygen through the (110), (111) and (100) single crystals of silver all fell along a linear Arrhenius plot with the activation

energy and the preexponential very similar to that found for the polycrystalline silver. This indicates that the transport limitation is approximately the same, even though there is some substantial difference in the microstructure. The magnitude of the diffusivity was found to be different for the three different crystal orientations which is inconsistent with the relation of K = DS since the solubility must be the same. The variation in the diffusivity can be explained by the relative displacement along a given crystallographic direction for a given number of jumps. The diffusivity ratios were in reasonable agreement with the ratio of the displacements squared.

The permeability for Ag0.05Zr alloy was found to be a fact of 1.86 higher than polycrystalline silver. The 0.05 percent Zr gives a much higher grain boundary and defect density to provide more reservoirs for oxygen which will increase the solubility and give the higher permeability. The diffusivity data has a higher activation energy but is very close in magnitude to the polycrystalline silver.

The effect of the surface limitation on the transport was further examined by using a glow discharge on the upstream side to enhance the formation of oxygen atoms. It was found that the flux of oxygen substantially increased from the steady state dissociative adsorption level by a factor of 6. This indicates that there is a definite surface limitation for normal dissociative adsorption. The increased signal during the glow discharge suggests that the adsorption and dissolution rate for oxygen atoms is substantially greater than for the previously conducted permeation experiments where O_2 molecules are dissociatively adsorbed.

ACKNOWLEDGEMENTS

I would like to thank Dr. G. S. Khandelwal, my advisor, for his help in preparing this manuscript. I would also like to thank Dr. R. A. Outlaw for his guidance and help in the accomplishment and subsequent relation of the research presented here.

TABLE OF CONTENTS

LIST OF FIGURES

CHAPTER I

INTRODUCTION

The transport of oxygen in and through silver has been studied over the past 70 years, primarily because of the technological importance of silver as a catalyst (e.g. the epoxidation of ethylene) and because of its unique solubility to oxygen. Ethylene oxide is primarily an intermediate stage for various organic syntheses, such as the production of solvents, artificial fibers, preparations for textiles, and detergents. To produce ethylene oxide, ethylene is transformed by reaction with atomic oxygen adsorbed on a silver surface (T = 250 °C) according to:

$$CH_2 = CH_2 + \frac{1}{2}O_2 \xrightarrow{Ag} CH_2 - CH_2 \quad (O)$$

The limitation to this reaction is the rate at which oxygen is dissociatively adsorbed and dissolved into the silver so that the surface concentration of atomic oxygen is maximized. This indicates that it is necessary to understand the transport properties of oxygen through silver.

Previous studies, however, reveal little insight into the fundamental mechanisms that control the transport. None of the studies have examined the transport through silver single crystals or silver alloys. Furthermore,

there has been no characterization of the microstructure in any of the previous studies, so it is unclear as to how the oxygen is partitioned into the silver bulk and what proportion of the transport proceeds by defect, grain boundary or lattice diffusion. In addition, there are no studies which describe the role that dissociative adsorption of the surface plays in the overall transport.

There are many diffusion mechanisms such as the interstitial mechanism, the interstitialcy mechanism, the crowdion mechanism, and the vacancy mechanism. However, the interstitial mechanism seems to be the most appropriate one for oxygen diffusion through silver because oxygen atoms primarily occupy the octahedral sites in the face centered cubic silver lattice. Since the interstitial sites are predominantly vacant, diffusion occurs more readily because when the thermal energy is available, jumps between interstices occur instantly since there is no need to wait for the arrival of a vacancy. In some cases the mechanism is obvious, but the simultaneous occurrence of interactions with defects, grain boundaries, or impurities can provide a much more complicated overall process.

In general, the process of permeation through metal membranes includes the following steps:

(1) Adsorption of the molecules on the high-pressure side of the membrane.

(2) Dissociation of the molecules to atoms.

(3) Incorporation of the atoms into the lattice, grain boundaries or defects.

(4) Diffusion through bulk by random walk migration.

(5) Emergence from solid solution at the low-pressure vacuum interface.

(6) Reassociation to molecules.

(7) Desorption.

Normally, the controlling step of permeation is step 4, i.e. diffusion of atoms through the bulk crystal structure. There are, however, other factors which may compete with this step, such as the dissociative adsorption of the oxygen molecule on the Ag surface. The number of investigations into the surface physics of oxygen on silver is quite extensive, but even in this area, the results are so different that no precise wisdom exists as to how molecules adsorb, dissociate and ultimately dissolve into the lattice, defects and grain boundaries of the silver. Since these steps are precursor states to bulk diffusion, it is essential to understand how these processes occur and whether there exist a limiting rate for oxygen to dissolve into the silver lattice.

Also, silver is well known to be very sensitive to impurities restricting grain growth, since the segregation of these impurities to the grain boundaries tends to slow down or stop intergranular transfer of silver atoms from smaller to larger grains. Past experiments have pointed

out that impurities could significantly effect the experimental results. Low purity silver will not yield reproducible results. Questions arise here as to how significantly the grain boundary density would effect the oxygen permeation through silver and how important a part does the grain boundary diffusion play in the overall transportation mechanism for the diffusion of oxygen in silver ? Furthermore, if interstitial diffusion is the dominant transport mechanism, is there an effect due to the crystalline orientations ?

In order to provide some understanding of the aforementioned questions, the objectives of this work were to study the permeation of oxygen through high purity large grain silver, through the (110), (111) and (100) single crystals of silver and through the selected alloy Ag0.05Zr. The alloy was chosen on the basis that Zr (a grain refiner) could be used to produce a fine grain crystal structure in order to evaluate the grain boundary and defect contribution to the overall transport. In addition, studies were also conducted using glow discharge dissociation of the supply side (upstream) molecular oxygen in order to examine whether the normal dissociative adsorption is a limiting step in the overall transport process.

CHAPTER II

SURVEY OF LITERATURE

Surface Properties

The surface interaction between oxygen and the silver surface has received much attention for the past 70 years mainly because of the high activity of silver for the selective epoxidation of ethylene. Almost all of the present understanding of this system were derived from surface studies of oxygen adsorption on the (100), (110), and (111) single-crystal surfaces of silver (refs. 1 to 20). The inconsistencies among these studies clearly indicate that chemically bound oxygen on silver is not well understood. These discrepancies seem to arise from the various oxygen exposure conditions used. The results of these studies are described briefly for each surface.

O/Ag(100). This surface is the least researched of the three. The sticking coefficient for oxygen on this surface is on the order of 10^{-5} to 10^{-6}. This is a very small value which suggests that the molecular orbitals of the oxygen are, in general repelled by the surface and most likely that adsorption only occurs at defects. Based on work function measurements, the existence of two binding states of oxygen on this surface has been tentatively proposed (refs. 1): one state which exist

alone at temperatures above 97 °C and a second state which increases in relative concentration with decreasing temperature. Oxygen exposure causes a decrease in the spot intensity of the 1 X 1 low-energy-electron diffraction (LEED) pattern of the clean surface. The appearance of new diffraction spots upon oxygen adsorption is a controversial topic. Two observations have been presented in the literature (ref.13). One observation claims that new diffraction spots appear, an occurrence which suggests that adsorption is either disordered or in a phase with a 1 X 1 silver structure. The second observation is that oxygen adsorption causes facets of the (410) plane to form which are inclined 14 degrees relative to the (100) surface domains. Regardless of the surface distribution that actually occurs, the overall surface concentration of oxygen is very low. Auger electron spectroscopy (AES) shows only a barely detectable oxygen signal (the minimum detectable concentration is about 1%) ~ 10^{13} atoms cm^{-2}. Thermal desorption of the adsorbed layer from this surface occurs near 240 °C.

O/Ag(110). The (110) surface is the most reactive toward oxygen with an initial sticking coefficient of approximately 10^{-3}. Although this is still a small value, the increased reactivity is probably because of the ribbed structure where only the O_2 molecules which are aligned with the valleys at the moment of collision are dissociatively adsorbed. It is also possible that there is a much higher defect density on this surface. The initial sticking coefficient decreases with increasing temperature, an occurrence which may provide evidence for a precursor state for

chemisorption of oxygen. Based on LEED patterns obtained with various exposures for a room-temperature oxygen exposed (110) surface, the maximum surface coverage is proposed to be half a monolayer ~ 5 x 10^{14} atoms cm^{-2}. In addition to the precursor state, three adsorbed states of oxygen have been proposed: an adsorbed dioxygen state, an adsorbed dissociated oxygen state, and a subsurface dissociated oxygen state. The dioxygen state has been most commonly observed at temperatures below -153 °C where van der Waals forces predominate and produces a diffraction pattern which indicates a 2 X 1 to 2 X 7 structure depending on the coverage. It has also been proposed that a dioxygen adsorbed state exists at 200 °C following oxygen exposures at or exceeding 0.1 torr. However, it is not clear if these dioxygen states are the same. The dissociated oxygen state is formed by exposure at temperatures equal to or greater than -103 °C or by heating an already exposed surface above -103 °C. This state is the most prominent adsorbed state of oxygen above -103 °C, but the binding site is unknown. None of the bonding models proposed today take into account probable adsorbate-induced surface reconstruction nor are they consistent with the available data. The subsurface dissociated oxygen which is stable to 327 °C, has been reported to form by heating an oxygen-exposed surface above 147 °C. Above 327 °C the surface and subsurface oxygen atoms combine and desorb as O_2. It has also been suggested that this subsurface oxygen migrates to the surface near 267 °C.

O/Ag(111). The (111) surface is similar in reactivity toward

oxygen to the (100) surface in that it has a sticking coefficient on the order of 10^{-6}. At temperatures below -123 °C the prominent surface species is O_2, which desorbs near -58 °C. This suggests as in the (100) case, that van der Waals forces are dominant. Above -58 °C the adsorbed state of oxygen is controversial. It is not clear whether an adsorbed dioxygen species exists above -58 °C. An exposure of 1 to 2 torr of oxygen in the range of 127 °C to 227 °C results in a diffraction pattern with a weak p(4 X 4) structure. This structure is stable to approximately 307 °C, where it associatively desorbs as O_2. As for the (110) surface, a subsurface state is proposed which desorbs above 327 °C.

In summary, past research on the surface properties for the O/Ag system shows a very small sticking coefficient and virtually no adsorption on the (100) and (111) planes and the maximum surface coverage is only about half monolayer on the (110) plane at room temperature (refs. 1 and 5). This indicates little oxygen affinity for adsorption on single crystal silver and suggests a barrier to oxygen dissolution into the bulk. Polycrystalline silver may contain all the binding states associated with the crystalline surfaces described above. In addition, states which may be associated with grain boundaries and other defects could be important. Therefore, studies of single-crystal surfaces may only offer a general indication of the behavior of a polycrystalline surface. In agreement with the single-crystal studies (subsurface oxygen desorbs at 450 °C), 490 °C is sufficient for desorption of the surface oxygen to occur. No surface-controlled phenomena appear to

limit the thermal evolution of oxygen from the surface.

Transport Properties

Although the number of investigations into the surface physics of oxygen on silver is quite extensive, very little work has been done on the transport properties of oxygen through silver. Generally speaking, The temperature curve for the solubility S of a gas in a metal is given by the equation:

$$S = S_0 \exp\left(-\frac{H}{RT}\right) \qquad 2.1$$

where S is the solubility coefficient, S_0 is an entropy factor and H is the solution enthalpy. Based on thermodynamic considerations, a monotomic function of temperature is expected for the enthalpy in the temperature range considered here. Hence it is most likely that there is a monotomic function for the temperature-solubility curve. All the metal-gas systems examined today seem to fit this picture. The deviations of solubility values from the square-root law at low temperatures and lower pressures obtained from previous studies suggest the same origin since the apparatus and test method allowed no distinction between solubility and adsorption.

Eichenauer and Muller (ref.21) studied polycrystalline silver in

1962 using the desorption technique which is based on observing the release of gas from a gas-charged metal body. The gas escaping from the metal is transferred to a collector vessel and the accumulation over time is tracked with pressure measurements. The diffusion and solubility can be calculated from the resulting gas release curves. The gas released from a metal usually follows the laws of volume diffusion, however, there are many processes with which the escape of an atomically dissolved gas from a solid can be effected. There is a risk that interface processes may govern or at least influence the gas release and hence cause misinterpretation of the results. To solve this problem, Eichenauer and Muller used specimens of different dimensions and shapes to find if there is surface interference upon desorption. All the specimens were prepared with 99.995% pure silver melted in a vacuum ($\sim 10^{-3}$ torr) in a quartz crucible, and poured into chills. Rolling and turning into three different sizes and shapes: cylinder with 0.53 cm diameter and 29.85 long, small spheres with 0.98 cm diameter and large spheres with 2.99 cm diameter. To remove surface impurities, all the specimens were pickled for 1 hour in a 10% aqueous solution of hydrochloric and tartaric acids. The oxygen used in the experiment was produced at 300 °C from potassium permanganate, condensed in a vessel chilled with liquid nitrogen and purified by repeated distillation, freezing out all expectable impurities. All the 38 measurements were performed in the temperature range between 412 °C and 863 °C at various pressures. The results are shown in Fig. 2.1 and Fig. 2.2. The solubility and diffusivity for oxygen in silver were found to obey the following relationships:

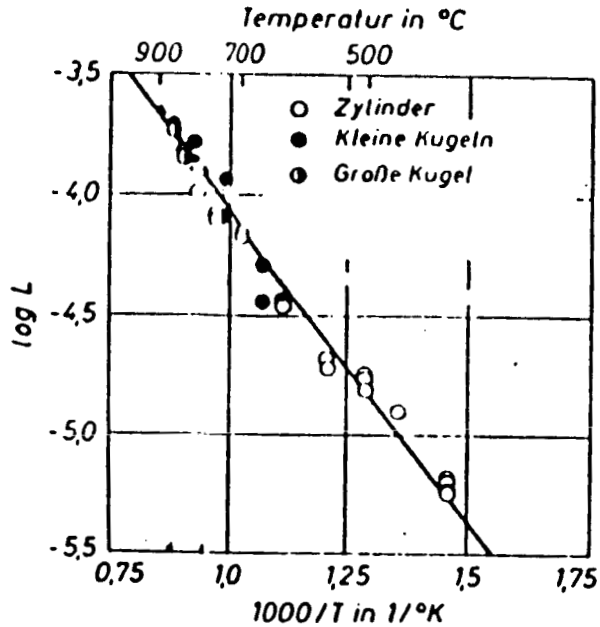

Fig 2.1 Permeability of oxygen in polycrystalline silver as a function of reciprocal temperature

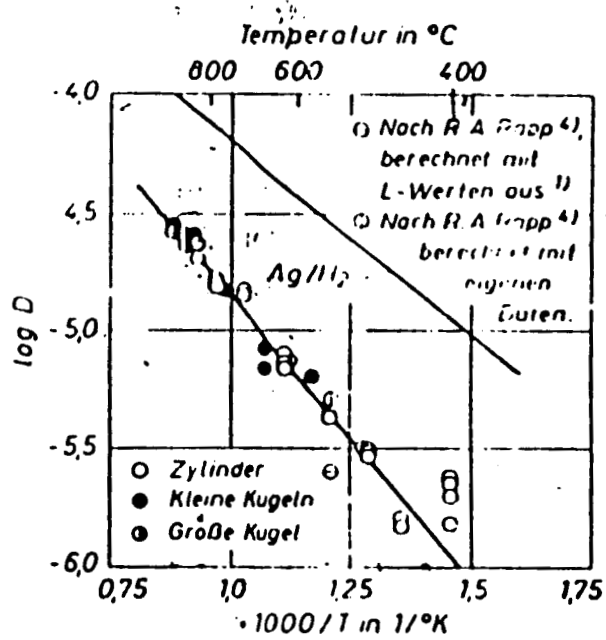

Fig 2.2 Diffusivity of oxygen in polycrystalline silver as a function of reciprocal temperature

$$S = 1.42 \times 10^{21} \exp\left(-\frac{11860}{RT}\right) \qquad 2.2$$

$$D = 3.66 \times 10^{-3} \exp\left(-\frac{11000}{RT}\right) \qquad 2.3$$

According to the measurements at constant temperature and different pressure, it was found that the " Sieverts " square root law ($C = SP^{1/2}$) applies to the solubility of oxygen in silver. The dissolution of oxygen and subsequent migration of oxygen ions through silver follows the dissociation of the oxygen molecules into atoms at the surface. Within the error limits, the gas release curves of all specimens followed the law of volume diffusion. The low solubility and very slow diffusion below 400 °C impeded measurements in this temperature range, most likely because of the increasing stability of the surface adsorption below 400 °C. Since it was found that the activation energy for diffusion is relatively low (11 kcal/mole), it was concluded that the diffusion takes place between interstitial sites.

Coles (1963) studied the permeability of silver to oxygen using the same desorption technique for the purpose of developing an oxygen gas leak for an accelerator ion source (ref.22). He did not address what kind of silver was used. The temperature range was between 500 °C and 850 °C.

He found that the process obeys the "Sieverts" square root law, the same as Eichenauer and Muller did. However, the permeability he obtained was almost one decade larger than what Eichenauer and Muller obtained. Silver is well known to be very sensitive to impurities which will restrict grain growth, since the segregation of these impurities to the grain boundaries tends to slow down or stop intergranular transfer of silver atoms from smaller to larger grains. Some experiments with refined silver (99.9% purity) did not yield reproducible results and subsequent microscopic examination revealed pores in the edge zone of the refined silver specimen. Since Coles did not mentioned the purity of the silver, the reason why his permeability is higher than Eichenauer and Muller's can not be determined. It is possible that his diffusion is greater due to defects and higher grain boundary density. If there was porosity, this could also result in an increased solubility. As studied by Coles, one of the convenient ways to eliminate many of the gas impurity problems is to introduce the desired gas through a permeation membrane which is specific to that gas alone, thus effecting a filtration of impure gas for the desired species. Nickel and palladium are used to purify and introduce hydrogen isotopes into a vacuum system. Vitreous silica is used as a helium membrane and silver is used to introduce oxygen. In order to examine the gas purity and system response of using silver to introduce oxygen, Beavis (1971) studied oxygen permeation through a silver tube at a temperature of about 550 °C (ref.23). A monopole gas analyzer was used to record the mass-spectra changes continuously during the experiment. It was found that silver could be heavily contaminated with

hydrogen, carbon, and sulfur, but after long periods of oxygen flow, the sulfur dioxide, the organic materials in the spectra, and also the carbon oxides decrease, subsequent to which the oxygen begins to flow at the expected steady state rate.

Ramanarayanan and Rapp (1972) studied the diffusivity of oxygen through silver at high temperature (750 °C - 950 °C) using the electrochemical technique (ref.24). The experiment consisted of a solid electrolyte tube with an external porous platinum electrode and the solid silver inside the tube. The silver was first melted and most of the oxygen was pumped out of it with an applied voltage of +1.5 V at 1100 °C. The furnace was then cooled at a rate of 15 °C to 20 °C per hour until solidification had proceeded from the bottom of the melt to the top. During solidification, the bottom of the metal was kept at about 10 °C lower than the top of the metal. After completion of the solidification, the cell portion of the tube was adjusted to be in the constant temperature zone of the furnace. Pump-out curves of cell current vs time were recorded using applied voltages in the range from 0 to 200 mV. During the experiment, an atmosphere of purified argon was maintained over the surface of the liquid or the solid metal. The experimentally determined values for the diffusivities and solubilities of oxygen in solid silver agreed closely with the values of Eichenauer and Muller's.

Gryaznov, Gul'yanova and Kanizius (1973) studied permeability and diffusivity of oxygen through polycrystalline silver at low temperature

using permeation technique (ref.25). A degassed silver tube (99.99 % purity) with length of 240 mm, outside diameter of 3 mm and the wall thickness of 0.2 mm was sealed within a glass sphere which contains a mass-spectrometer. The system was first evacuated till the oxygen peak intensity indicated by the mass spectrometer was less than 0.03 volts. Then the oxygen was admitted into the tube and the increase of the oxygen peak was recorded till the equilibrium was established. With the known temperature, pressure difference and the time, the diffusivity and permeability was calculated. The temperature range was between 250 °C and 400 °C. The permeability and the diffusivity were found to obey the follow relationships:

$$K = 5.92 \times 10^{18} \exp\left(\frac{-20356}{RT}\right) \qquad 2.4$$

$$D = 4.67 \times 10^{-4} \exp\left(\frac{-8093}{RT}\right) \qquad 2.5$$

The values of the activation energies are significantly lower than that obtained in previous research.

Outlaw, Sankaran, Hoflund and Davidson (1988) studied permeability and diffusivity of oxygen through large grain polycrystalline silver membranes under ultrahigh vacuum conditions (ref.26). Data was obtained over the temperature range between 400 °C and 800 °C. The specimen was prepared with 99.9999% pure silver melted in a vacuum (10^{-8} torr) and spark machined into a disk geometry with 1.07 cm diameter

which means that less contaminated silver has been used compared to that of previous researchers. The permeability and diffusivity were determined directly from experiment and the solubility determined by calculation (Eichenauer and Muller determined the solubility and diffusivity from experiment and from which, the permeability was obtained). It was found that above 630 °C the permeability and diffusivity closely agree with Eichenauer and Muller, but below 630 °C, they found a change in slope of the diffusivity curve and the activation energy for diffusion is considerably higher than that of Eichenauer and Muller. Outlaw found that this could probably be explained by the higher efficiency of trapping at the lower temperatures. This trapping effect has also been observed for hydrogen in iron and hydrogen in alloyed copper (ref. 27).

In summary, very little work has been done to provide insight into the fundamental mechanisms that control the transport and none of the aforementioned studies have examined the oxygen permeation through single crystal silver or silver alloys. Actually, only one study exists for the permeation of any gas through any single crystals and this was hydrogen permeation through Pd(110) (ref. ??). Furthermore, there has been no characterization of the microstructure in any of the previous studies. It is unclear as to how the oxygen is partitioned and what proportion the transport proceeds by defect, grain boundary or lattice diffusion.

CHAPTER III

THEORETICAL ANALYSIS

Thermodynamics

Atoms that normally reside in interstitial positions diffuse through silver by making a series of elementary jumps to nearest neighbor interstitial positions. The simplest form of the diffusion equation are regarded as purely phenomenological descriptions relating the rate of flow of matter to its concentration gradient known as Fick's first law:

$$J = - D_i \nabla C_i \qquad 3.1a$$

and

$$\frac{\partial C}{\partial t} = D_i \nabla^2 C_i \qquad 3.1b$$

known as Fick's second law. Where J, the flux, is the number of particles passing through a plane of unit area per unit time, C is the concentration, and the D are the diffusion coefficients (or diffusivity) along the three principal crystallographic axes.

In one dimensional case, consider two adjacent lattice planes located at x and x + dx as shown in figure 3.1. Suppose the concentration of the oxygen atoms per unit area at x is N_x and is N_x + dx at x+dx. Let all the diffusing atoms be of the same element; hence, D is independent of concentration. Further, the atoms are restricted to diffusive jumps between nearest neighbor positions, which is generally the case for all real solids. Then, the flux of atoms moving from left to right is given by

$$J_x = \frac{1}{2} \Gamma N_x \qquad 3.2$$

and from right to left by

$$J_{x+\Delta x} = \frac{1}{2} \Gamma N_{x+\Delta x} \qquad 3.3$$

where Γ, the mean jump frequency, is the average number of times that an atom changes lattice sites per second.

Therefore, the net flux expressed in terms of concentration per unit area is given by

$$J = J_{x+\Delta x} - J_x = \frac{1}{2} \Gamma (N_{x+\Delta x} - N_x) \qquad 3.4$$

and in terms of concentration per unit volume and the concentration gradient

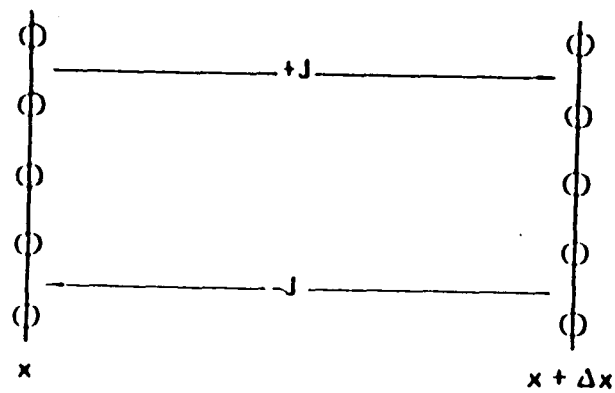

Fig 3.1 Adjacent lattice planes illustratin one-dimensional diffusion in which atoms exchange positions by jumping Δx

$$J = \frac{1}{2}\Gamma(\Delta x)\frac{N_{x+\Delta x} - N_x}{\Delta x} = \frac{1}{2}\Gamma(\Delta x)\frac{\Delta N_x}{\Delta x} \qquad 3.5a$$

Replacing $\Delta N/\Delta x$ by the concentration ΔC and passing to the limit

$$J = \frac{1}{2}\Gamma(\Delta x)^2\frac{\partial C}{\partial x} \qquad 3.5b$$

Because Δx, the lattice spacing, is very small compared to the total diffusion path, we can pass to the limit and (3.5a) reduces to (3.5b) where Δx is in fact the distance of separation of nearest neighbors, a.

$$J = -\frac{1}{2}\Gamma a^2\frac{\partial C}{\partial x} \qquad 3.6$$

The extension of this derivation to octahedral interstitial sites is done by taking the appropriate values of Γ along each of the six principal crystallographic axes. Since Γ and the distance between nearest interstitial neighbors along all principle axes must be the same

$$J = -\frac{1}{12}\Gamma a^2\frac{\partial C}{\partial x} \qquad 3.7$$

If (3.7) is compared with equation (3.1), we can see that for a FCC crystal (where the distance of the lattice spacing along the six principal crystallographic axes are the same), D equals:

$$D = \frac{1}{12}a^2\Gamma \qquad 3.8$$

Since the interstitial diffusion requires that a vacant site be adjacent to the diffusing atom, it is necessary to multiply the right hand side of (3.8) by the probability that the diffusion atom possesses nearest neighbor vacancy.

$$D = \frac{1}{12} a^2 \Gamma X_v \qquad 3.9$$

where X_v is the atom fraction of the interstitial vacancies. This formalism does not include any correction for orientation effects.

In terms of classical thermodynamics, we can consider interstitial sites to behave as though they were a very dilute solute which forms an ideal solid solution with the host lattice. The change in entropy is then simply the ideal entropy of mixing:

$$S_m = - R [N_v \, Ln \frac{N_v}{N} + N_a \, ln \frac{N_a}{N}] \qquad 3.10$$

where S_m is mixing entropy; N_a is the mole of the oxygen atoms; N_v is the mole of interstitial vacancies; N is the total mole of the interstitial sites and R is the gas constant.

For the standard Helmholtz free energy of formation of the vacancies, we have

$$F_v = N_v (\Delta E_v - T\Delta S_v) + TS_m \qquad 3.11$$

where F_v is free energy due to vacancies; E_v is internal energy per mole vacancies; S_v is the vibrational entropy per mole vacancies.

This free energy must be a minimum if the crystal is in equilibrium, that is, the number of vacancies in the crystal will seek the value that makes free energy a minimum at any given temperature

$$\frac{\partial F_v}{\partial N_v} = \Delta\mu_v = \Delta E_v - T\Delta S_v + RT \ln\frac{N_v}{N} = 0 \qquad 3.12$$

where μ_v is the chemical potential.

At equilibrium, $\mu_v = \mu_v^o$, and we can identify ΔE_v and ΔS_v as the standard internal energy and entropy of formation respectively, ΔE_v^o and ΔS_v^o. Thus we finally obtain

$$\Delta E_v^0 - T\Delta S_v^0 + RT \ln\frac{N_v}{N} = 0 \qquad 3.13$$

Now since $X_v = \frac{N_v}{N}$, then

$$X_v = \exp\left(-\frac{\Delta E_v^\circ - T\Delta S_v^\circ}{RT}\right) \qquad 3.14$$

Because vibration energy $T\Delta S_v^o$ is small compared to internal energy ΔE_v, equation (3.14) is frequently written as

$$X_v \approx \exp\left(-\frac{\Delta E_v^{\circ}}{RT}\right) \qquad 3.15$$

Substituting equation (3.15) into (3.9), we have:

$$D = \frac{1}{12} a^2 \Gamma \exp\left(-\frac{\Delta E_v^{\bullet}}{RT}\right) \qquad 3.16$$

Although (3.1a) is useful in some fields, it seldom provides a convenient basis from which to calculate the diffusivity of atoms in a solid, as there is seldom an easy way to directly measure a flux except the diffusion of a gas into or out of a solid. Generally, the experimenter allows the diffusion to proceed for a fixed period of time, then halts it abruptly. This permits calculation of D by solving the equation known as Fick's second law:

$$\frac{\partial C}{\partial t} = D_i \nabla^2 C_i \qquad 3.17$$

Consider three adjacent lattice planes labeled as shown in figure 3.2 where concentration is a function of position and time, and the time rate of change of the concentration per unit area at position x is given by

$$\frac{\partial N_x}{\partial t} = \frac{N(t + \Delta t, x) - N(t, x)}{\Delta t} \qquad 3.18$$

Now the total number of atoms arriving at a plane x is given by

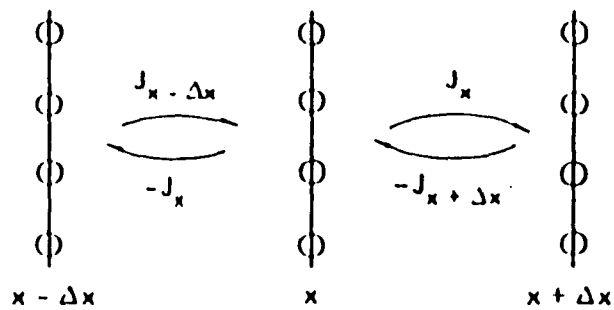

Fig 3.2 Three adjacent lattice planes illustrating one-dimensional diffusion in which atoms exchange positions by jumping Δx

$$N_+ = \frac{\Gamma}{2} [\, N_{x-\Delta x}\Delta t + N_{x+\Delta x}\Delta t \,] \qquad 3.19$$

and number leaving is

$$N_- = \Gamma N_x \Delta t \qquad 3.20$$

Subtracting (3.20) from (3.19) and multiplying above and below by dx gives

$$\frac{N_+ - N_-}{\partial t} = \frac{N_x}{\partial t} = \frac{\Gamma}{2} (\Delta x)^2 \frac{N_{x-\Delta x} - 2N_x + N_{x+\Delta x}}{(\Delta t)^2} \qquad 3.21$$

Converting to concentration and passing to its limit

$$\frac{\partial C}{\partial t} = \frac{1}{2} \Gamma(\Delta x)^2 \frac{\partial^2 C}{\partial x^2} = D \frac{\partial^2 C}{\partial x^2} \qquad 3.22$$

which is the one dimensional version of (3.17). Equation (3.22) is, in effect, the result of taking the second finite difference in the concentration gradient and equating it to the time dependent flow of atoms at a fixed point.

Permeation Kinetics

The permeation through a planar membrane is generally described by reference 28. From Fick's second law, we have the relation

$$\frac{\partial C}{\partial t}(x,t) = D\frac{\partial^2 C(x,t)}{\partial x^2} \qquad 3.23$$

where x is the variable distance through the membrane and t is the time.

The equation (3.23) may be solved for the following boundary conditions:

$$C(x, t=0) = g(x) \qquad 3.24$$

$$C(x=0, t) = S P_0^{1/2} = C_1 \qquad 3.25$$

$$C(x=d, t) = S P_d^{1/2} = C_2 \qquad 3.26$$

where g(x) is an arbitrary function, d is the membrane thickness, S is the solubility, P_0 is the high-side pressure, and P is the pressure at the ultra-high vacuum interface, which is usually taken to be zero at the beginning of the experiment. In equations (3.25) and (3.26), the " Sieverts " square root law was applied and 1/2 power was assumed, which indicates that the oxygen migrates through the solid as atoms.

Considering the above conditions, the solution to equation (3.23) is (ref.29)

$$C(x,t) = C_1 + (C_2 - C_1)\frac{x}{d} + \frac{2}{\pi}\sum_1^{\infty}\left[\frac{C_2\cos n\pi x - C_1}{n}\right]\sin\frac{n\pi x}{d}\exp\left(-\frac{Dn^2\pi^2 t}{d^2}\right)$$

$$+\frac{2}{d}\sum_1^{\infty}\sin\frac{n\pi x}{d}\exp\left(-\frac{Dn^2\pi^2 t}{d^2}\right)\int_0^d g(x)\sin\frac{n\pi x}{d}\,dx \qquad 3.27$$

Now, if at t=0 vacuum is on both sides of the membrane, then g(x)=0. If the upstream side of the membrane is pressurized, $C_1 = SP_O^{1/2}$, $C_2 = 0$, and equation (3.27) becomes

$$C(x,t) = C_1 \left[1 - \frac{x}{d} - \frac{2}{\pi} \sum_1^{\infty} \frac{1}{n} \sin \frac{n\pi x}{d} \exp\left(- \frac{Dn^2\pi^2 t}{d^2} \right) \right] \qquad 3.28$$

According to the Fick's first law, the gas flux J then is

$$\begin{aligned} J(x=d,t) &= -D \left(\frac{\partial C}{\partial x} \right)_{x=d} \\ &= \frac{DSP_0^{1/2}}{d} \left[1 + \frac{x}{d} - 2 \sum_1^{\infty} (-1)^n \exp\left(- \frac{Dn^2\pi^2 t}{d^2} \right) \right] \end{aligned} \qquad 3.29$$

which for large time is

$$J(x=d, t \to \infty) = \frac{DSP_0^{1/2}}{d} = \frac{KP_0^{1/2}}{d} = J_{eq} \qquad 3.30$$

where the permeability K=DS.

For the vacuum system being used, we have the relationship

$$f = \frac{Q}{n - n'} \qquad 3.31$$

where f is the conductance between downstream side of the membrane and

the ion pump; Q is the throughput or gas flux; n is the downstream number density and n' is the ion pump number density.

Since n is much larger than n', (3.31) can be written as

$$f \approx \frac{Q}{n} \qquad 3.32$$

Using the ideal gas relation

$$P_{eq} = nkT \qquad 3.33$$

and since $Q = J_{eq}A$, then

$$J_{eq} = \frac{P_{eq}f}{AkT} \qquad 3.34$$

Combining equation (3.34) and (3.30), we obtain the permeability equation

$$K = \frac{P_{eq}fd}{P_0^{1/2}AkT} \qquad 3.35$$

In order to determine the diffusivity following the establishment of a steady-state permeation rate, the upstream or high-pressure side can be reduced to zero such that $C_1 = C_2 = 0$, and the concentration through the membrane with rest time t = 0 is

$$C(x, t=0) = g(x) = SP_0^{1/2}\left(1 - \frac{x}{d}\right) \qquad 3.36$$

thus equation (3.27) becomes

$$C(x, t) = \frac{2}{d}\sum_{1}^{\infty} \sin\frac{n\pi x}{d} \exp\left(-\frac{Dn^2\pi^2 t}{d^2}\right) \int_0^d SP_0^{1/2}\left(1 - \frac{x}{d}\right) \sin\frac{n\pi x}{d}\, dx \qquad 3.37$$

which yields

$$C(x, t) = \frac{2SP_0^{1/2}}{\pi}\sum_{1}^{\infty} \frac{1}{n} \sin\frac{n\pi x}{d} \exp\left(-\frac{Dn^2\pi^2 t}{d^2}\right) \qquad 3.38$$

and the flux is

$$J(x = d, t) = \frac{KP_0^{1/2}}{d}\left[-2\sum_{1}^{\infty} (-1)^n \exp\left(-\frac{Dn^2\pi^2 t}{d^2}\right)\right] \qquad 3.39$$

Now if $D_t >> 10^{-4}$, then the ratio of the first and second terms is $J_{n=2}/J_{n=1} \approx 0.01$ and J(x=d,t) can then be written as

$$J(x = d, t) = \frac{2KP_0^{1/2}}{d} \exp\left(-\frac{D\pi^2 t}{d^2}\right) \qquad 3.40$$

Dividing equation (3.40) by (3.30) gives the normalized flux

$$\frac{J}{J_{eq}} = 2\exp\left(-\frac{D\pi^2 t}{d^2}\right) \qquad 3.41$$

The time varying total flux AJ(t) and pressure P(t) within the system are related by

$$V\frac{dP(t)}{dt} = AkTJ(t) - f\,[\,P(t) - P'(t)\,] \qquad 3.42$$

where V is the volume of the measurement chamber and P(t) is the time varying pressure within the pump.

Since P(t) >> P(t), then

$$J(t) = \frac{V}{Akt}\frac{dP(t)}{dt} + \frac{f}{AkT}P(t) \qquad 3.43$$

A worst case condition occurs at high temperatures when dP(t)/dt is greatest, but even at 800 °C the ratio of the first term on the right-hand side to the second term is less than 0.02, so the flux can be written as

$$J(t) = \frac{f}{AkT}P(t) \qquad 3.44$$

We can now say that

$$\frac{J(t)}{J_{eq}} \approx \frac{P(t)}{P_{eq}} \qquad 3.45$$

Combining the ratio of (3.45) with (3.41) gives

$$\frac{P(t)}{P_{eq}} = -2\sum_{1}^{\infty}(-1)^{n}\exp\left(-\frac{Dn^2\pi^2 t}{d^2}\right) \qquad 3.46$$

where D is the diffusivity. Experimentally, the time for $P(t)/P_{eq} = 0.1$ can be determined, and we can find D by numerical iteration of equation (3.46).

CHAPTER IV

Experimental Apparatus

Vacuum system

Since the permeation technique used in this work requires the use of ion gauges and a mass spectrometer which can only operate below 10^{-4} torr because of e^- scattering by the gas density, and since the impurity of the gas could significantly contaminate the silver membrane and effect the adsorption and desorption of oxygen on the silver surfaces, it is necessary to conduct the experiment in a system which was capable of achieving ultrahigh vacuum (P ~ 10^{-11} torr). At this background pressure, it would take 15 hours before a monolayer of contaminant (e.g. carbon from CO, CO_2 or CH_4) could compromise the data. Experiment times were always less than 8 hours. The vacuum system used here was an all metal sealed system made of 304L stainless steel capable of being baked up to 450 °C. The chamber and associated apparatus are shown in figure 4.1 and schematically in figure 4.2. As shown in the schematic, the main components which comprise the system are: a 500 liter/second diode ion pump, a titanium sublimation pump, a 20 liter/second triode pump, an oil-free molecular drag pump backed by a diaphragm pump, a capacitance manometer gauge, an ionization gauge and a qradrupole mass spectrometer

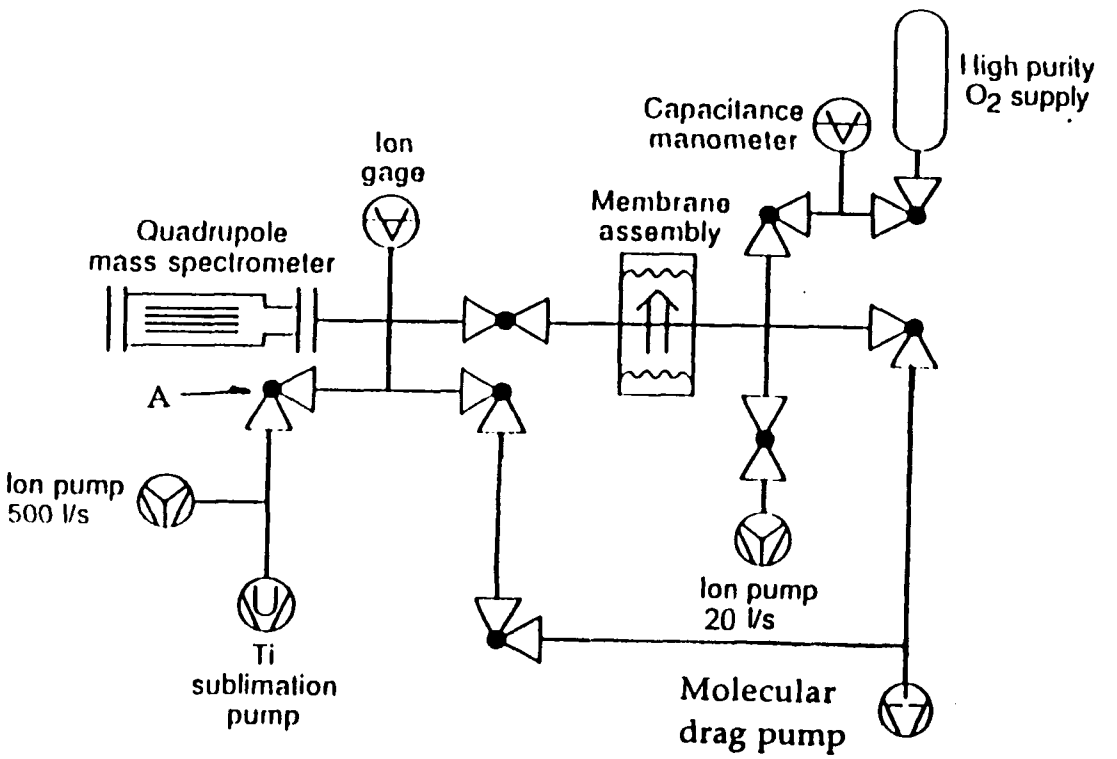

Fig. 4.2 Schematic of the ultra-high vacuum permeation system

(QMS). The 304L stainless steel hardware that constituted the system envelope was previously vacuum fired at 600 °C for 16 hours to minimize the hydrogen outgassing rate. The 500 liter/second diode ion pump and the titanium sublimation pump were employed on the downstream side; the 20 liter/second triode pump was pumping on the upstream side to permit appropriate cleanup of the high pressure side of the membrane surface and of the oxygen gas supply line; the oil-free molecular drag pump was used to evacuate the system from atmosphere to 10^{-6} torr and also used as the upstream pump during the experiments. The ion gauge was used to measure the downstream pressure and the capacitance manometer gauge was used to measure the upstream pressure. A small calibrated conductance f was used to separate the measurement chamber from the main ion pump in order to provide a known conductance limitation and therefore a known flow rate out of the measurement chamber. Measurement of the pressure, P(t), then allowed the determination of the permeating flux J(t). Figure 4.3 shows the valve for the calibrated conductance f. Valve A has two positions: open and close. During bakeout, it was open (about 8 liter/second) to facilitate maximum pumping speed to the main ion pump. After bakeout and during permeation runs, the valve was in the closed position, which provided a 0.7 liter/second calibrated conductance for oxygen flow through the valve.

A heater assembly (comprised of beaded NiCr wire) was designed to control the temperature of the silver membrane. An ion gauge was used to measure the total pressure of the downstream side of the membrane since

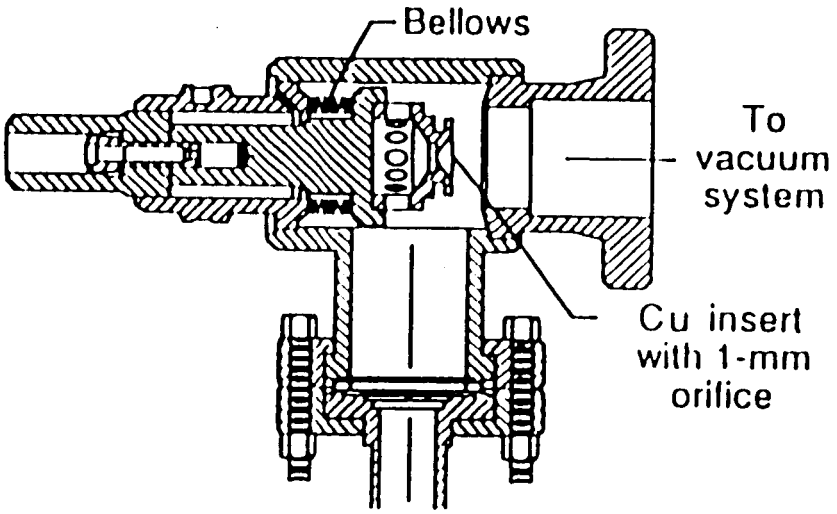

Fig. 4.3 Conductance limiting valve

it is easy to calibrate. The output of the ion gauge was connected to a logarithmic picoammeter (K 26000) which was calibrated by a standard picoampere source (K 261) and a digital multimeter (Fluke 2344) and the output from the picoammeter was recorded by a strip chart recorder (HP 7132A). An UTI 100C quadrupole mass spectrometer was used to detect the oxygen partial pressure on the downstream side of the membrane as a reference for equilibrium since it has higher sensitivity compared to the ion gauge. The QMS was also used to determine when contamination in the gas phase was minimized. The output of the QMS was recorded on the same strip chart recorder. A MKS capacitance manometer was used to measure the total pressure of the upstream side of the membrane.

The Ion Gauge

The ion gauge consists of a nude closed end Bayard-Alpert type ionization gauge (Varian) and control unit (Varian Ionization Gauge 971-0003). The ionization gauge contains three elements: filament, grid, and collector as shown in figure 4.4. The filament serves as source of electrons, the grid functions as the electron collector operating at a positive potential (+130 volts) with respect to the filament, and along the axis of the cylindrical grid structure is a very small diameter ion collector which operates at zero potential. Electrons from the filament

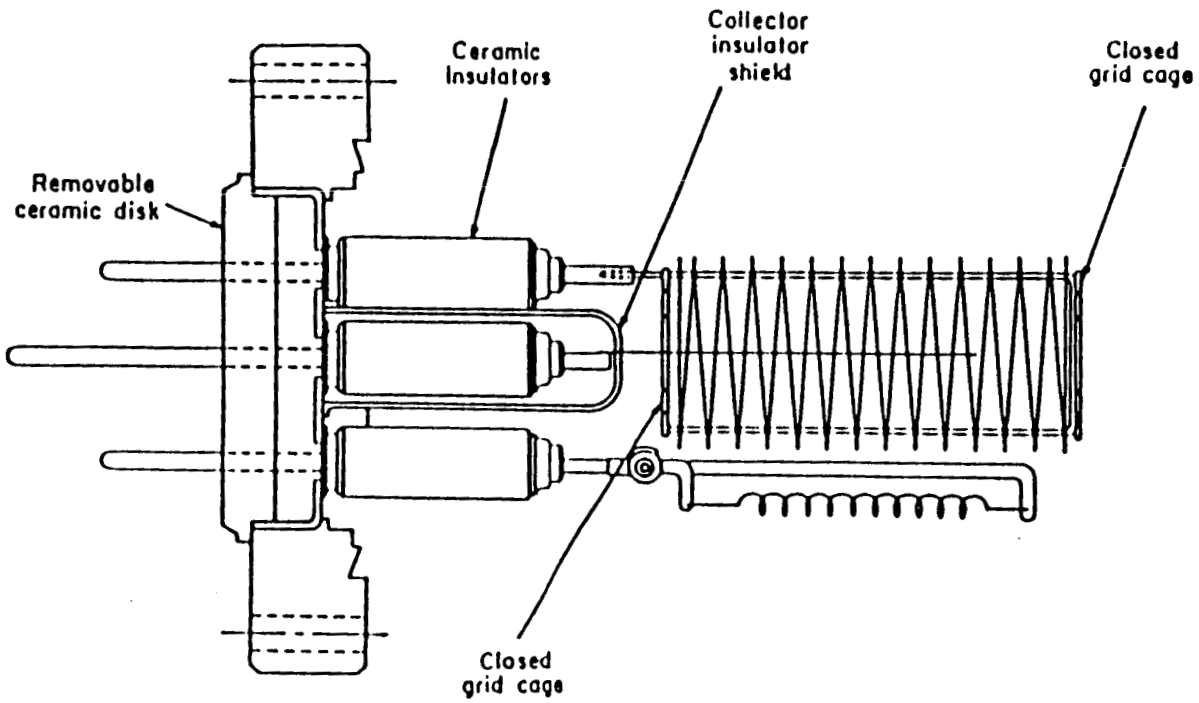

Fig. 4.4 Nude Bayard-Alpert ionization gauge with closed grid cage

pass through the grid several times on the average before being collected at the grid. While passing through the interior of the grid structure the electrons ionize gas molecules at a rate which is proportional to the gas density. The positive ions produced on the inside of the grid structure are accelerated toward and neutralized at the collector by electrons from the external circuit. The number of ions produced per electron is proportional to gas density, and the positive ion current to the ion collector is used as and indication of pressure. Thus, for a constant value of accelerating voltage in excess of the ionization potential of the gas, the number of positive ions formed should vary linearly with pressure and the electron current. This is described by the relation:

$$S = \frac{1}{P} \times \frac{i_c}{i_g} \qquad 4.1$$

where i_c is the ion current in amps to the collector, i_g is the electron current in amps to the grid, and P is the pressure in torr. The sensitivity, S, called the gauge constant in units of $torr^{-1}$, is the proportionality constant. For a given electron emission current, sensitivity and a measured ion current, P can be calculated. The ion gauge employed in this work has a sensitivity of 30 $torr^{-1}$. This is higher than the 25 $torr^{-1}$ of the sensitivity of the regular gauge because it is enclosed in a high conductance metal envelope. This instrument was the primary downstream pressure measurement, P(t), because its dynamic response was superior to that of the QMS.

The Quadrupole Mass Spectrometer

The QMS consists of three section: the RF generator, the probe, and the control console. The primary components within the analyzer probe are the ionizer, the quadrupole mass filter and the electron multiplier as shown schematically in figure 4.6. The gas molecules within the ionizer are bombarded by electrons from the tungsten filaments and become positively charged ions by electron impact. The ions are then focussed into the mass filter. A combined radio-frequency and electrostatic field is formed by two pairs of metal rods in the filter section. A charged substance with a specific mass-to-charge ratio will have a dynamically stable trajectory within the field formed by the voltages on the rods while all other substances will be filtered out. By continuously varying the applied voltages, a mass range of 1 - 300 AMU can be analyzed. At a particular set of voltages, the ion with a specific m/e value can traverse the length of the filter. These ions arrive at the multiplier and are amplified into an electron current that is 10^6 times the ion current. The output current of the amplifier is referenced against the scan voltage which is in term referenced to a specific m/e of the ions, thereby producing a spectrum of peaks.

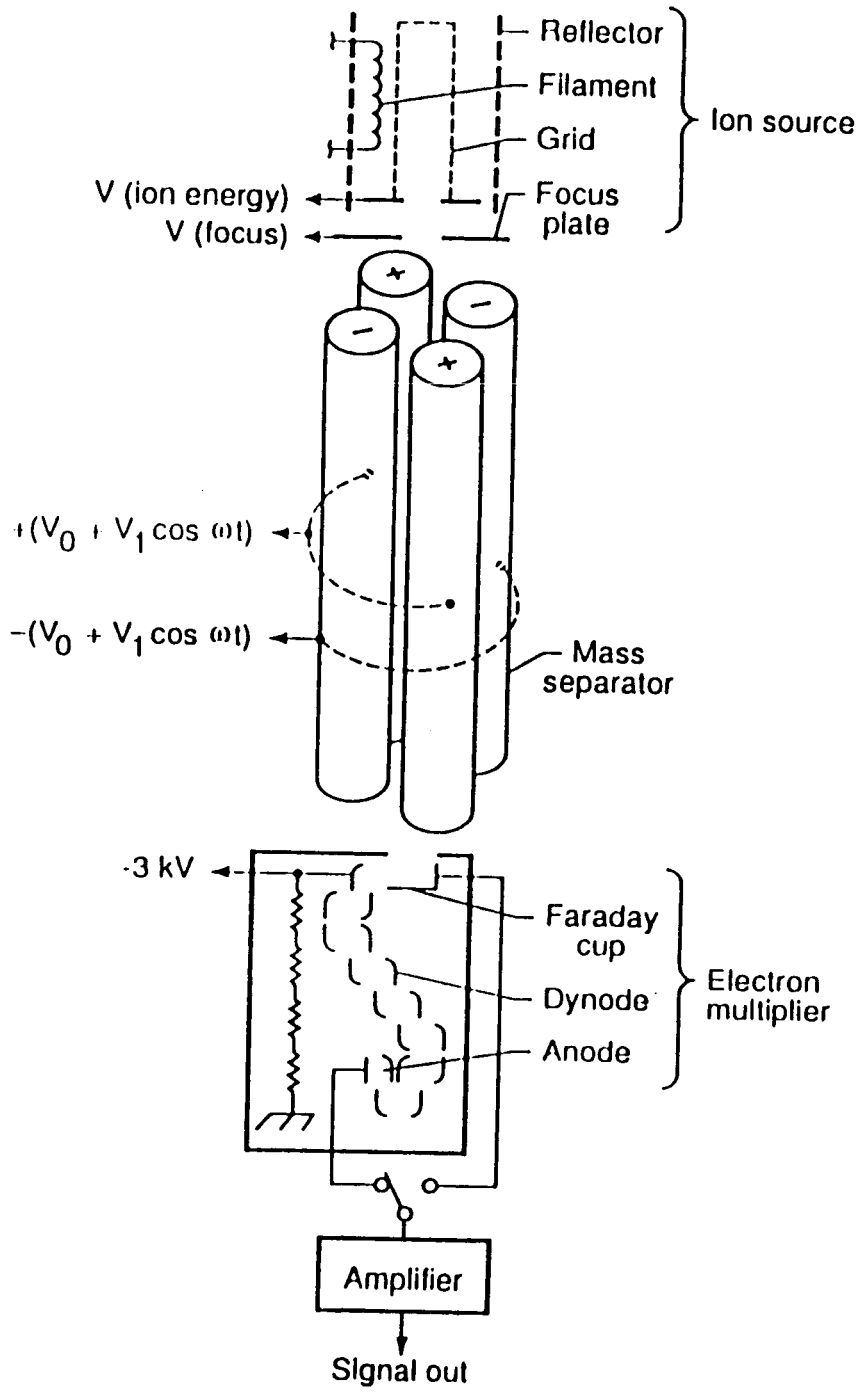

Fig. 4.5 Schematic of the analyzer probe

Ion Source

The ionizer used here is similar to one used in the ion gauge and at low emission current (0.5 mA); it is described in equation 4.1. The primary differences between an ion gauge and a quadrupole mass spectrometer ionizer are the ion extraction and focusing into the quadrupole mass filter section required by the latter. The ultimate resolution is very sensitive to the energy and entrance angles of the incoming ions to the quadrupole mass filter. Furthermore, the ionizer is designed to minimize the X rays that might transit the filter section to the detector and limit the detectability at low pressures.

Quadrupole mass filter

Ions formed in the ionizer and injected into the electrical quadrupole along the Z-axis of the quadrupole. The rods of the quadrupole are energized with a constant dc potential V_0 and an RF potential $V_1 \cos Wt$ (ref.30). The ions are subjected to a potential of the form

$$\Phi = (V_0 + V_1 \cos \omega t) \frac{x^2 - y^2}{r_0^2} \qquad 4.2$$

where V_0 is the dc voltage, V_1 is RF voltage, r_0 is the radius of the inscribed cross-sectional area of the quadrupole, and x,y are spatial

coordinates of cross section. The equations of motion for the ions are

$$m\ddot{x} + 2e\,(V_0 + V_1 \cos \omega t)\frac{x}{r_0^2} = 0 \qquad 4.3$$

$$m\ddot{y} + 2e\,(V_0 + V_1 \cos \omega t)\frac{y}{r_0^2} = 0 \qquad 4.4$$

and

$$m\ddot{z} = 0 \qquad 4.5$$

Equations 4.3 to 4.5 are Mathieu's differential equations. A transformation of coordinates is introduced as follows:

$$\omega t = 2\mu \qquad 4.6$$

$$a = \frac{8eV_0}{mr_0^2\omega^2} \qquad 4.7$$

$$b = \frac{4eV_1}{mr_0^2\omega^2} \qquad 4.8$$

The solutions of the differential equation in z are trivial. The solutions in x and y are infinite series of two types: the stable solution, for which x and y remain finite for all values of μ, and the unstable solution, for which x and y become infinite as $\mu \rightarrow \infty$. The stability of the solutions depends on the values of a and b. Figure 4.6 shows two regions: (1) ions that fall outside the triangular-shaped area enter unstable oscillations and are collected at the quadrupole electrodes, and (2) ions that fall

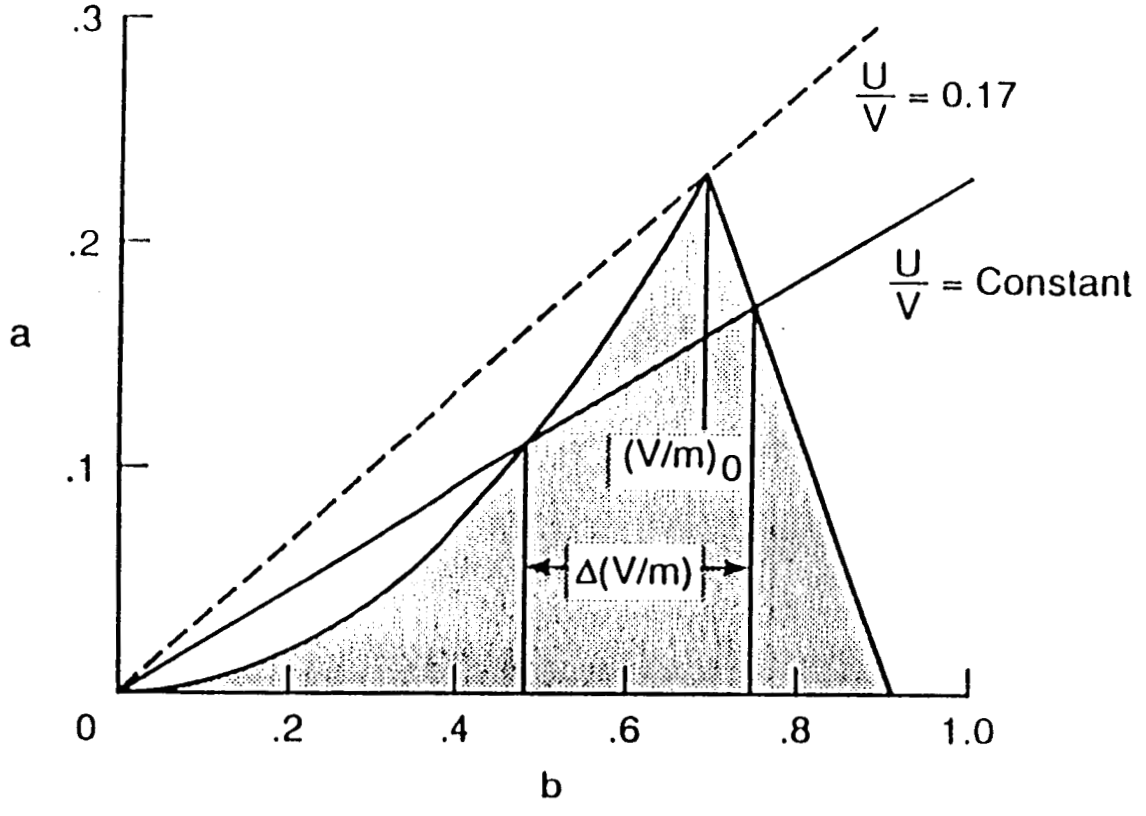

Fig. 4.6 Quadrupole operation: stable paths (transmitted) for ions in shaded area

inside the shaded area oscillate with amplitudes less than r_0 and pass through the analyzer.

The apex of the stability region occurs at b = 0.706, a = 0.23699, and $V_0/V_1 \approx 0.17$. At this point, only one mass, given by equation

$$m = \frac{2.85eV_1}{\omega^2 r_0^2} \qquad 4.9$$

$$V_0 \approx 0.17V_1 \qquad 4.10$$

will pass through the analyzer; the resolution is ∞ . For practical use, a lower value of V_0/V_1 is selected. The mass range is scanned by varying the RF and dc voltage level and keeping their ratio constant. A constant frequency is used and the resolution varies as 1/m. Certain boundary conditions on entrance aperture and entrance energy are required for optimum resolution.

Electron multiplier

The electron multiplier used here is a 16 stage electron multiplier. The discrete-dynodes are a Cu 2 - 4% Be alloy which forms a BeO surface layer. These multipliers can have a gain greater than 10^6 at approximately 100 V per stage. Ions exiting the mass separator are accelerated to the first dynode that is negatively biased 1 to 3 kV. Upon colliding with the dynode, the ions emit, on the average, several electrons per electron.

These electrons are attracted to the next dynode with an accelerating potential of 100 to 300 V. where each electron emits, on the average, several more electrons. This process continues through each of the stages until 10^4 to 10^8 electrons from a single ion appear at the collector in a pulse of current. This instrument was used to qualitatively indicate the gas composition (upstream and downstream) and to insured that contamination was minimized before data was taken.

The Capacitance Manometer Gauge

The capacitance manometer gauge consists of two absolute pressure sensors (MKS Baratron 122A) and a power supply digital readout (MKS PDR-C-2C). One of the absolute pressure sensors measures from 10^{-3} torr to 10 torr and the another from 10 torr to 1000 torr. The absolute pressure sensor is simply a diaphragm gauge as shown in figure 4.7. The pressure inlet tube connected to a small chamber in the sensor body. One wall of this chamber is a thin metal diaphragm which faces a rigidly mounted ceramic disc containing two electrodes in a volume which is permanently evacuated and sealed. When pressure is applied to the diaphragm, its deflection produces a change in distance between the electrodes and diaphragm which produces corresponding changes in capacitances. The control unit applies an AC signal to the electrodes. The changes in signal strength produced by the diaphragm are amplified and

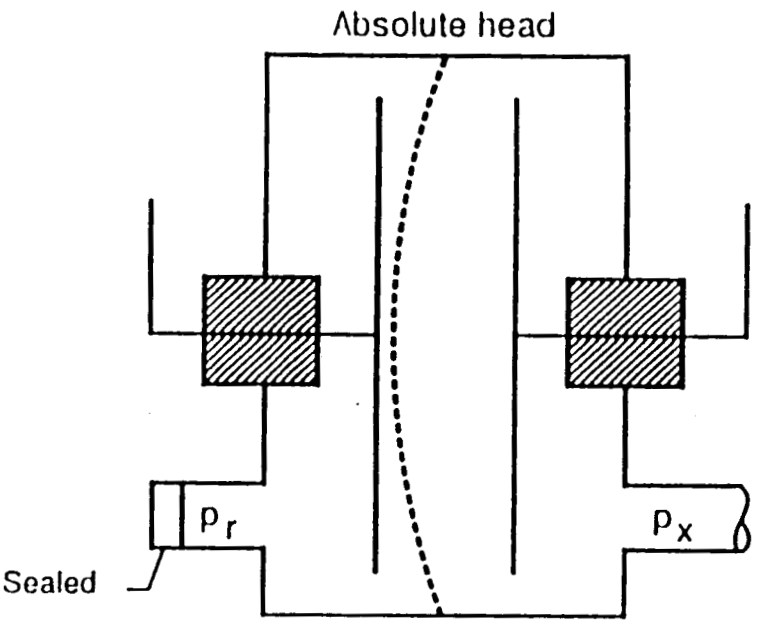

(a) $p_r << p_x$.

Fig. 4.7 Schematic of absolute capacitance manometers
P_r = Reference pressure; P_x = Unknown pressure

demodulated in phase to minimize the noise level. The DC output is then used to drive a digital readout. The digital readout can automatically cover the whole pressure range of the two sensors. The block diagram is shown in figure 4.8. This instrument has a dynamic range of 10^5 and provided measurement of P_0 from atmosphere to 10^{-3} torr.

The Heater Assembly

The heater assembly consists of NiCr heating wire with 0.02" diameter, insulation, cooling system, and temperature measurement as shown in figure 4.9. The heating wire has the resistance of about 60 Ω connected to a power source (Sstaco 003-2558 power source) with output range from 0 to 140 volts. The temperature of the membrane was controlled by the electric current through the heating wire. The temperature of the membrane was measured by a thermocouple (0.13 mm chromel-alumel) attached to the membrane and a readout (Fluke 2190A digital thermometer). The cooling system consisted of two external copper blocks mounted on each side of the insulated heater spool connected to teflon tubes in which was circulated refrigerated water from a KMC Laser Cooler which maintains the water at 60 °F.

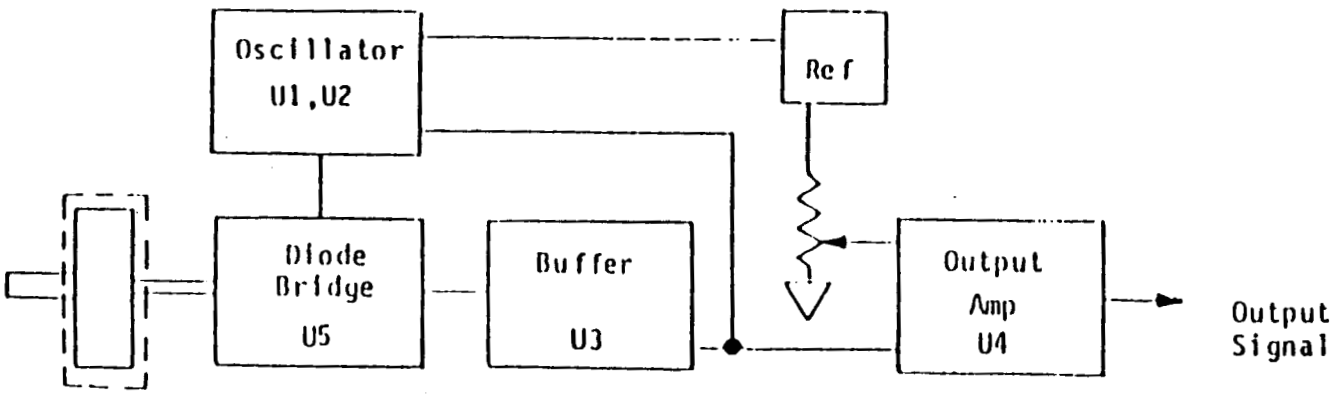

Fig. 4.8 The block diagram of the capacitance manometer gauge

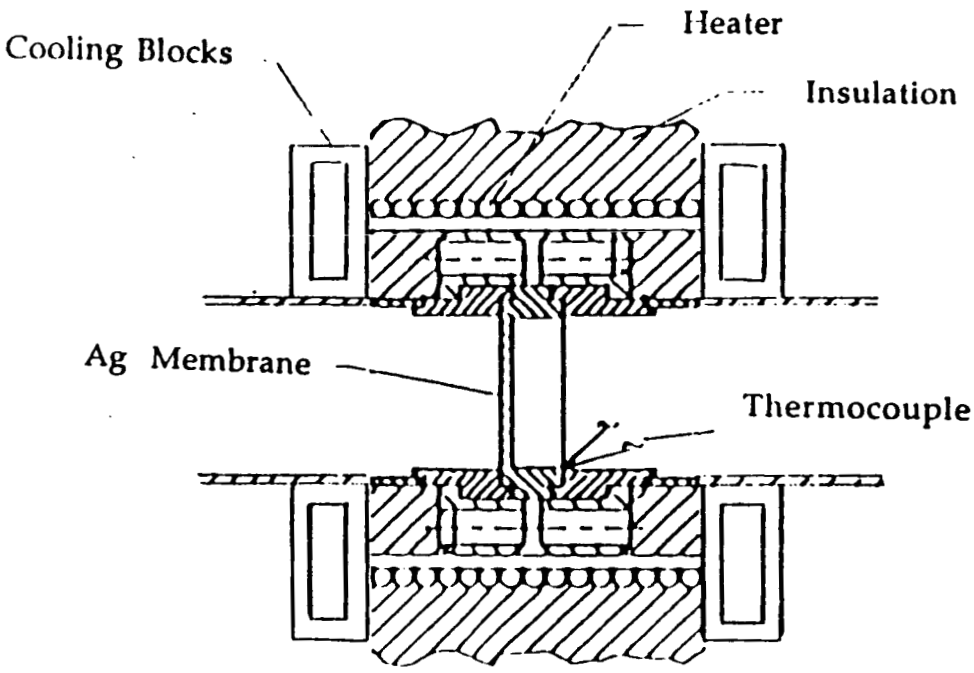

Fig. 4.9 Membrane heater assembly

The Samples

The (110), (111), and (100) single crystal silver membranes were purchased from Atomergic Chemetals Corp.. The purity of these single crystal silver was 99.9999%. The polycrystalline silver membrane and the alloy silver membrane were prepared with 99.9999+ percent purity silver that was melted in the vacuum environment (10^{-8} torr) and then spark machined into the disk geometry. The geometry of the silver membranes is shown in figure 4.10.

After the surface preparation, the membrane was immediately mounted between two flanges and installed into the system to minimize the contamination from the atmosphere. The flanges were spot welded from the outside because the high temperature operation was found to cause leaks at the seal due to the creep in the fastener bolts at 800 °C.

The membrane surface were prepared as shown in the following

1. Polished	30 μm grit finish
2. Degreased	Laboratory detergent in ultrasonic cleaner
3. Rinsed	Deionized water in ultrasonic cleaner

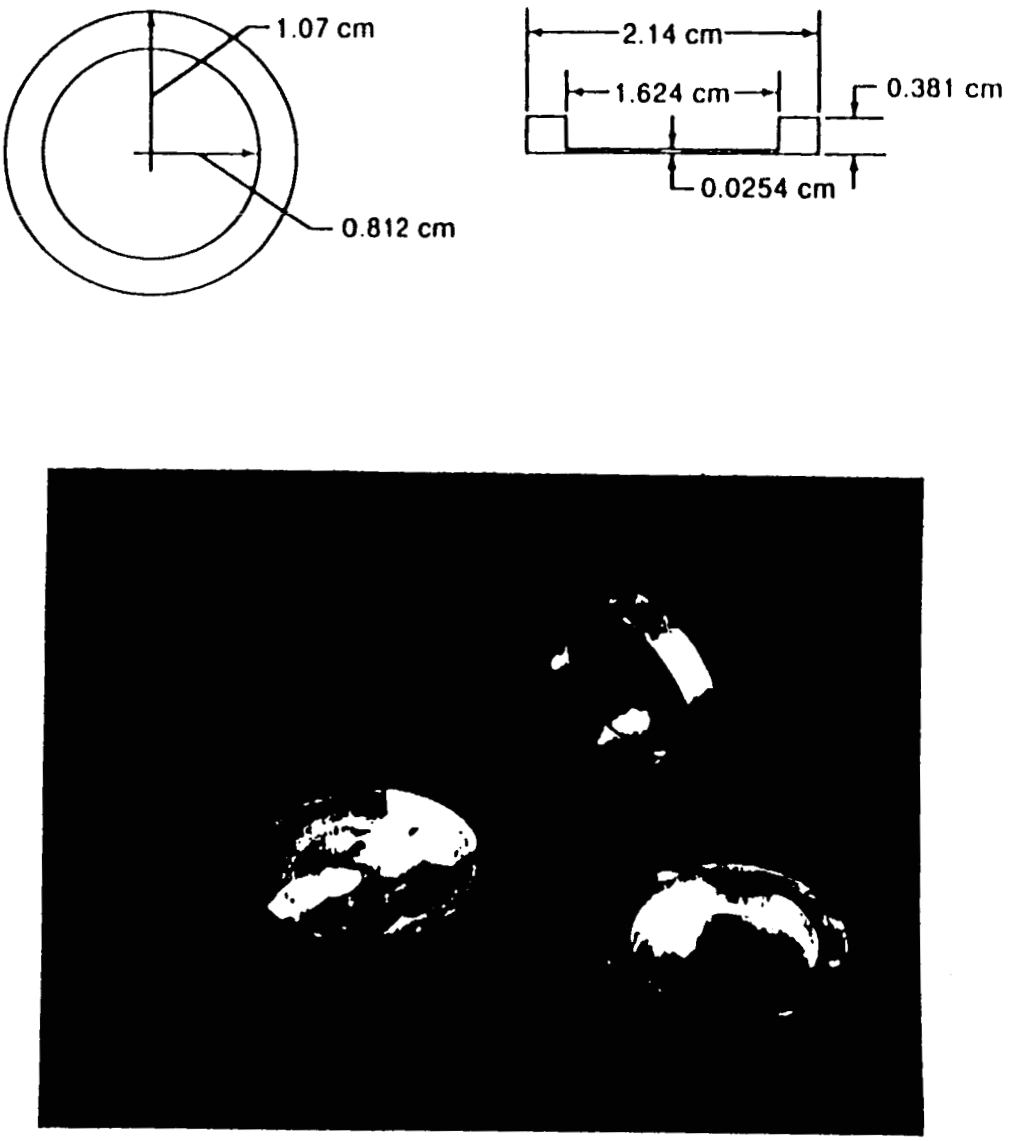

Fig. 4.10 Geometry of silver permeation membranes

4.	Chemically cleaned	4 parts HNO_3 to 1 part deionized water
5.	Rinsed	Deionized water
6.	Dried	Oil-free and filtered N_2

Attempts at electropolishing the silver were only successful with about one out of five membranes and left as much or more surface contamination than the chemical cleaning with the HNO_3 solution. Auger electron spectroscopy (AES) analysis of the surface conducted after the cleaning procedure is shown in figure 4.11 and closely resembles the spectrum of the sputter-cleaned silver surface. Small contaminant levels of S, Cl, C, and O can be observed, but the S, Cl, and C peaks were easily removed during the first few permeation runs of oxygen through the membrane. Figure 4.12 shows the microstructure of the large grain polycrysalline samples. No unusual preferential orientation was observed. The average grain size was found to be approximately 1.2 mm with some degree of twinning also observed.

The Oxygen Gas

The oxygen gas used in this experiment is research grade oxygen made by Air Products and Chemical Inc. The minimum purity is 99.995%. For this experiment, it was further purified by passing the gas through a

cold trap of dry ice and isopropyl alcohol. The purity of the gas was checked by the mass spectrometer and verified to be high purity.

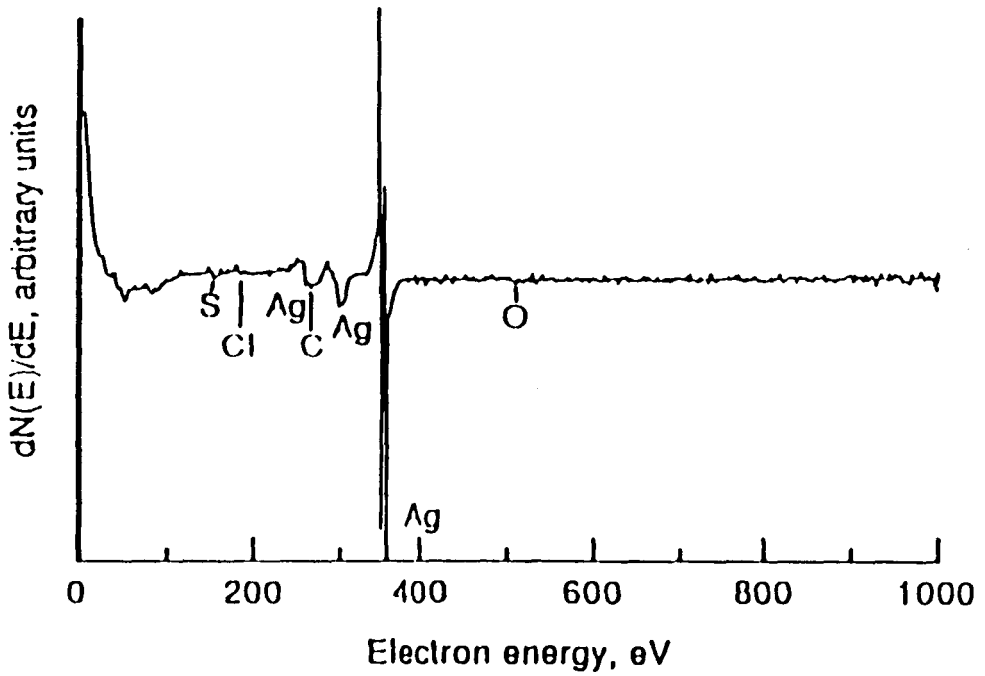

Fig. 4.11 AES survey of Ag membranes after polishing and chemical cleaning

Fig. 4.12 Microstructure of the polycrystalline silver membrane

CHAPTER V

Experimental Procedure

After the sample assembly was leak checked, it was mounted onto the system and leak checked again. Once the vacuum was assured, the pump down was initiated.

Pumpdown Procedure

The system was first roughed down to 10^{-4} torr using the molecular drag pump and then the 500 liter/second ion pump and 20 liter/second ion pump were started. The ion pumps reduced the pressure to 10^{-7} torr. The system bakeout was then initiated using a temperature ramp of about 25 °C per hour up to about 300 °C. This temperature was maintained for at least three days and then cooled down at the same rate to room temperature. Figure 5.1 shows the high-vacuum pumpdown of an unbaked, metal-gasketed system. In the initial stages the pressure is reduced exponentially with time as the volume gas is removed. Then the surface desorption and diffusion control the rate of pressure decrease. It can been seen from the figure 5.1 that the surface desorption and diffusion controlled pressure decreasing rate is so slow at room temperature that the permeation controlled pressure decreasing can never be reached on a practical time scale. The high-temperature processing (bakeout) can

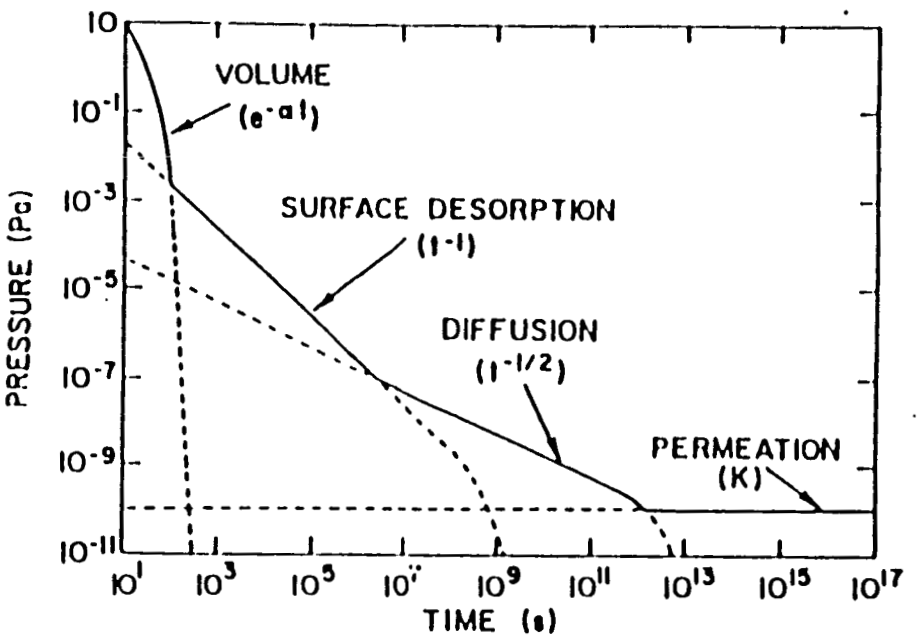

Fig. 5.1 Rate limiting steps during the pumping of a vacuum chamber

significantly increase the surface desorption and diffusion rate, so it is a necessity if ultrahigh vacuum is to be attained after a reasonable pumping time. The purpose of maintaining the elevated temperature during the heating period is to deplete the hydrogen concentration in the metal bulk and to oxidize the external surface (Cr_2O_3) to minimize the overall outgassing rate. This system had been previously baked to 450 °C so the lower temperature bake was sufficient to remove the surface H_2O and most of the other adsorbed species. During bakeout, valve A was open (8 liter/second) to facilitate maximum pumping speed to the main ion pump. After cooling to room temperature, the titanium sublimation pump was operated several times (45 amps for 1 min) and the ultimate pressure of the system was achieved (the 10^{-11} torr range).

Procedure for the Measurement

After the system had been baked and pumped down to its residual pressure of about 10^{-11} torr, the ion gage was degassed at the emission current of 100 mA and the quadrupole mass spectrometer was degassed at the emission current of 2.5 mA. The degas operation is necessary because the outgassing of H and O from the bulk and the surface of the hot filament of the ion gage and quadrupole mass spectrometer while in operation could significantly reduce the operation vacuum pressure obtainable. The membrane was then heated up to 800 °C by monitoring the electric current through the heating assembly. This procedure thoroughly vacuum degassed

the membrane. The logarithmic picoammeter was then calibrated by the standard picoampere source, a digital multimeter and a strip chart recorder. The valve which connects the 20 liter/second ion pump to the upstream side the membrane was closed and the absolute pressure gage was zero adjusted. The emission current of the ion gage and the quadrupole mass spectrometer were reduced to 0.4 mA and 0.5 mA respectively (normal operation is 4.0 mA and 2.5 mA respectively) in order to minimize instrument pumping.

The background gas spectra at room temperature, before and after introducing 10 torr oxygen into the high-pressure side of the system, appeared to be normal for stainless steel systems that have been vacuum fired and then baked out for several days. There was no significant O_2 signal and no change observed in the signal even when the high-side pressure was increased to 100 torr O_2 as shown in figure 5.2(a). However, as shown in figure 5.2(b), the O_2 peak substantially increased and became the dominant signal when the silver membrane was heated. The data shown in figure 5.2(b) correspond to equilibrium conditions for a silver temperature of 750 °C.

Permeability and Diffusivity Measurements

After vacuum degassing the membrane at 800 °C the valve which connect the roughing pump to the upstream side of the membrane was

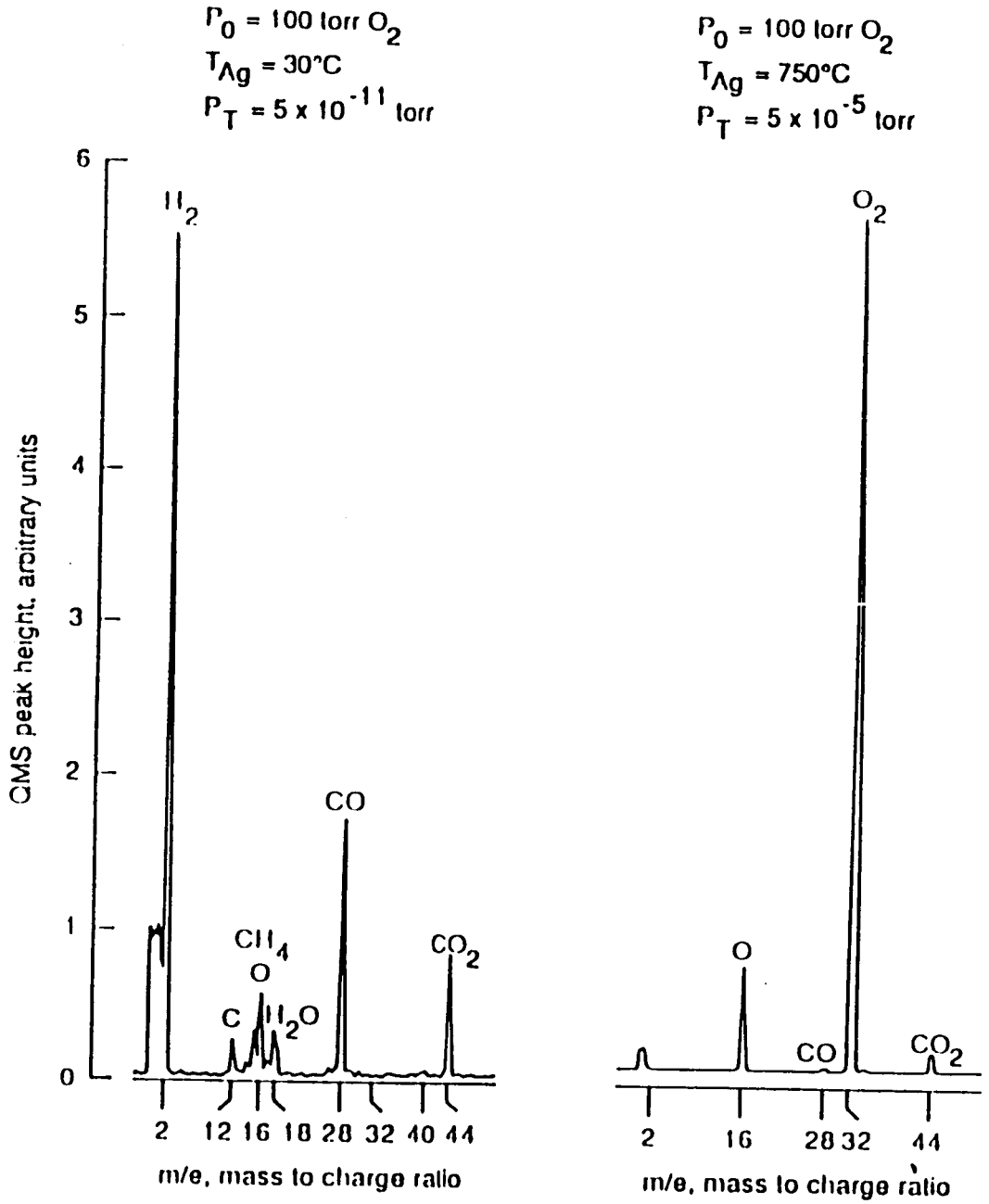

(a) Ag membrane at room temperature; P_0 = 100 torr O_2 (upstream pressure).

(b) Ag membrane at 750°C; P_0 = 100 torr O_2 (upstream pressure).

Fig. 5.2 QMS spectra of the permeation system

closed and oxygen was admitted to the high-pressure side up to about 150 torr. This upstream pressure was maintained until the quadrupole mass spectrometer indicated that the equilibrium flow had been established. Then, the upstream pressure was removed by opening the valve connecting to the roughing pump to determine the pressure decay in the downstream side of the membrane. This procedure was very effective in cleaning the membrane on both faces and was conducted several times before taking the data.

The data were taken at about 25 °C decrements over the temperature range of 400 °C to 800 °C by monitoring the signals of both the ion gage and QMS. First the temperature was established, then the valve connecting to the upstream side was closed and oxygen was admitted to the upstream side of the membrane. After the quadrupole mass spectrometer indicated that the equilibrium flow had been established, the membrane temperature, upstream pressure and ion current of the ion gage were recorded. The upstream pressure was then removed by opening the valve connecting to the roughing pump and the decay of the ion current of the ion gauge was recorded on the strip chart recorder. The ion current of the ion gauge was converted to downstream pressure by equation 4.1, and together with the upstream pressure and the decay of the downstream pressure, the permeability and diffusivity were calculated using the equation 3.35 and equation 3.46 for that specific temperature point. Figure 5.3 shows representative data for oxygen breakthrough to equilibrium (T_{Ag} = 600 °C, P_0 = 150 torr O_2) and then pressure decay (T_{Ag} = 600 °C, P_0 -> 0 torr O_2).

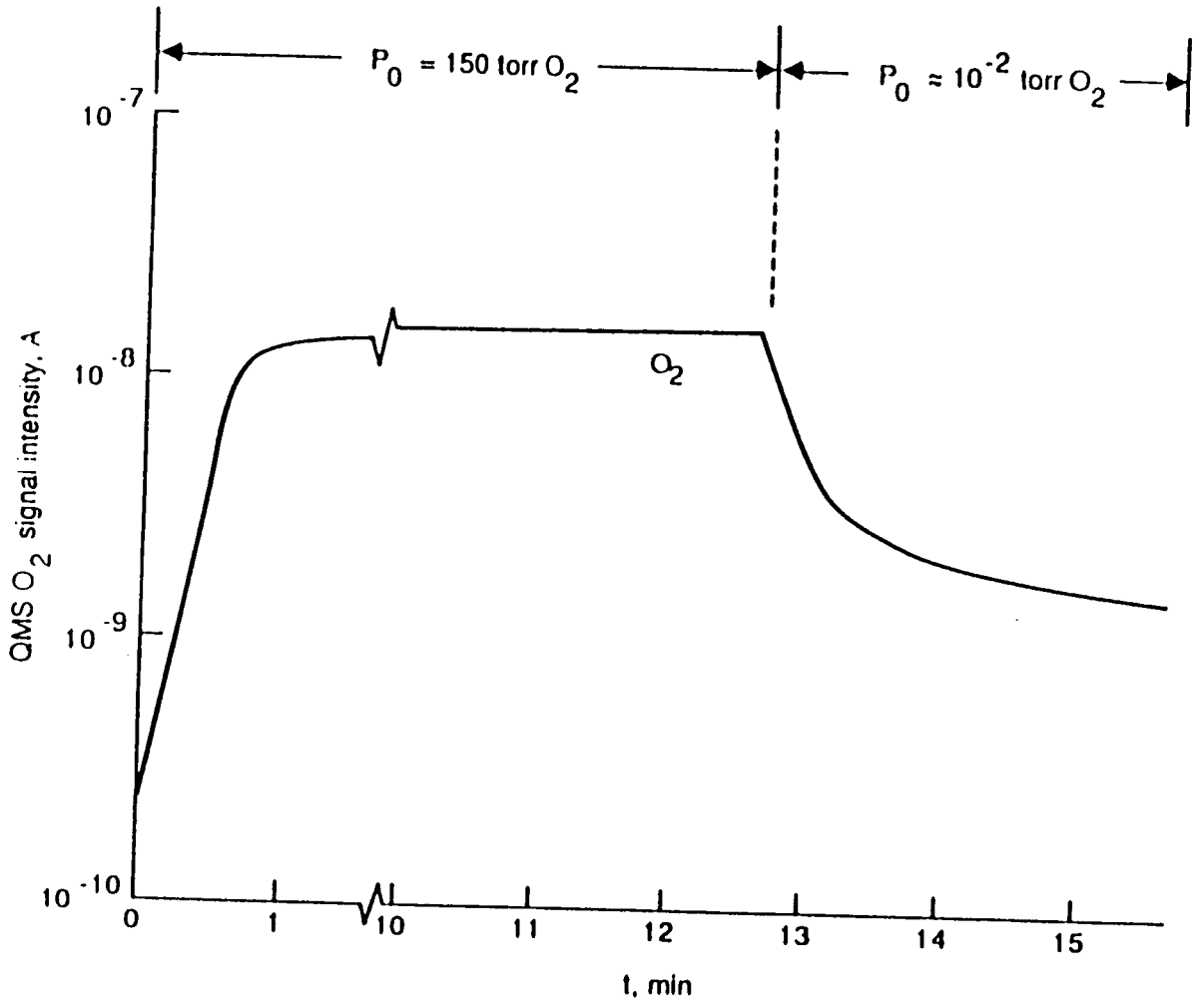

Fig. 5.3 Breakthrough and decay of oxygen through Ag membrane (T = 600 °C)

The pressure decay method was used to calculate the diffusivities for O/Ag, since it was experimentally simpler to establish equilibrium for a given P_0 and then open a pump valve to reduce the pressure to $P_0 = 0$. It avoided the "shock" of the hot silver membrane with a differential pressure of up to 150 torr and avoided surface limitations of a bulk property. In this method, it was observed that the diffusivity data were independent of upstream pressure for all pressures above 50 torr, although the reason for the weak dependency below 50 torr is not yet clear. The curvature that occurs after the linear decay in the signal is due to the incorporation of oxygen into the stainless steel walls of the vacuum system at equilibrium. When the high-pressure side is evacuated, a linear decay occurs as predicted by equation 3.46; but ultimately, as the pressure descends toward the background level, the data begin to curve because the charged walls now see an opposite concentration gradient that causes oxygen to desorb into the gas phase. This increase in oxygen gas flux results in an increased background pressure, but is substantially less than gas flux evolving from the membrane immediately after the high-pressure side is evacuated, so it does not alter the linear decay necessary to determine the diffusivity. This effect has also been substantiated by separate experiment.

At the higher temperatures studied, the vapor pressure of the silver is sufficiently large to cause some material loss from the membrane. For example, at 800 °C the vapor pressure is approximately 5×10^{-5} torr, which results in a sublimation rate of 0.01 mm/h. This represents a

significant mass loss and required corrections for each experimental run.

Glow-discharge measurements

The grow-discharge characteristics was observed for polycrystalline silver at a temperature of 650 °C. Oxygen was admitted to the high-pressure side of the membrane up to 0.5 torr. This upstream pressure was maintained until the quadrupole mass spectrometer indicated that the equilibrium flow had been established. Then, a 350 V DC and 50 mA current which was required for this geometry were applied to the upstream side of the membrane and maintained till the equilibrium was established again. The glow-discharge would extinguish at currents below 20 mA. A significant increase in the downstream flux was recorded by the change of the ion current of the ion gauge on the strip chart recorder at the same time. After that, the power was cut off and the valve connected to the roughing pump was open. The decay of the ion current of the ion gauge was then recorded. This cycle was repeated many times at 0.5 - 1.0 torr. Pressures above 2 torr were sufficient to extinguish the discharge, however.

CHAPTER VI

Results

Figure 6.1 shows the permeability vs upstream pressure from 0.5 to 250 torr for the (111) single crystal silver at a constant temperature of 650 °C. Note the permeability data approaches a constant value for upstream pressures larger than 50 torr. Similar behavior was also observed for polycrystalline silver. Based on these results, no upstream pressures (P_0) lower than 75 torr were used in this research (except for the glow discharge experiments).

Permeation and diffusion coefficients were calculated from equation 3.30 and equation 3.46 for all the different silver membranes: polycrystalline silver, the (111), (110) and (100) single crystals of silver, and the Ag0.05Zr alloy. The data are presented in the form of Arrhenius plots where some include the data of six separate runs. Several initial runs were required for each silver membrane, however, before the data became repeatable, presumably because of contaminant removal by the oxygen. The permeability equation and diffusivity equation were determined by least-squares fit of the data from the plots.

Polycrystalline Ag

The permeation data for the polycrystalline silver membrane was

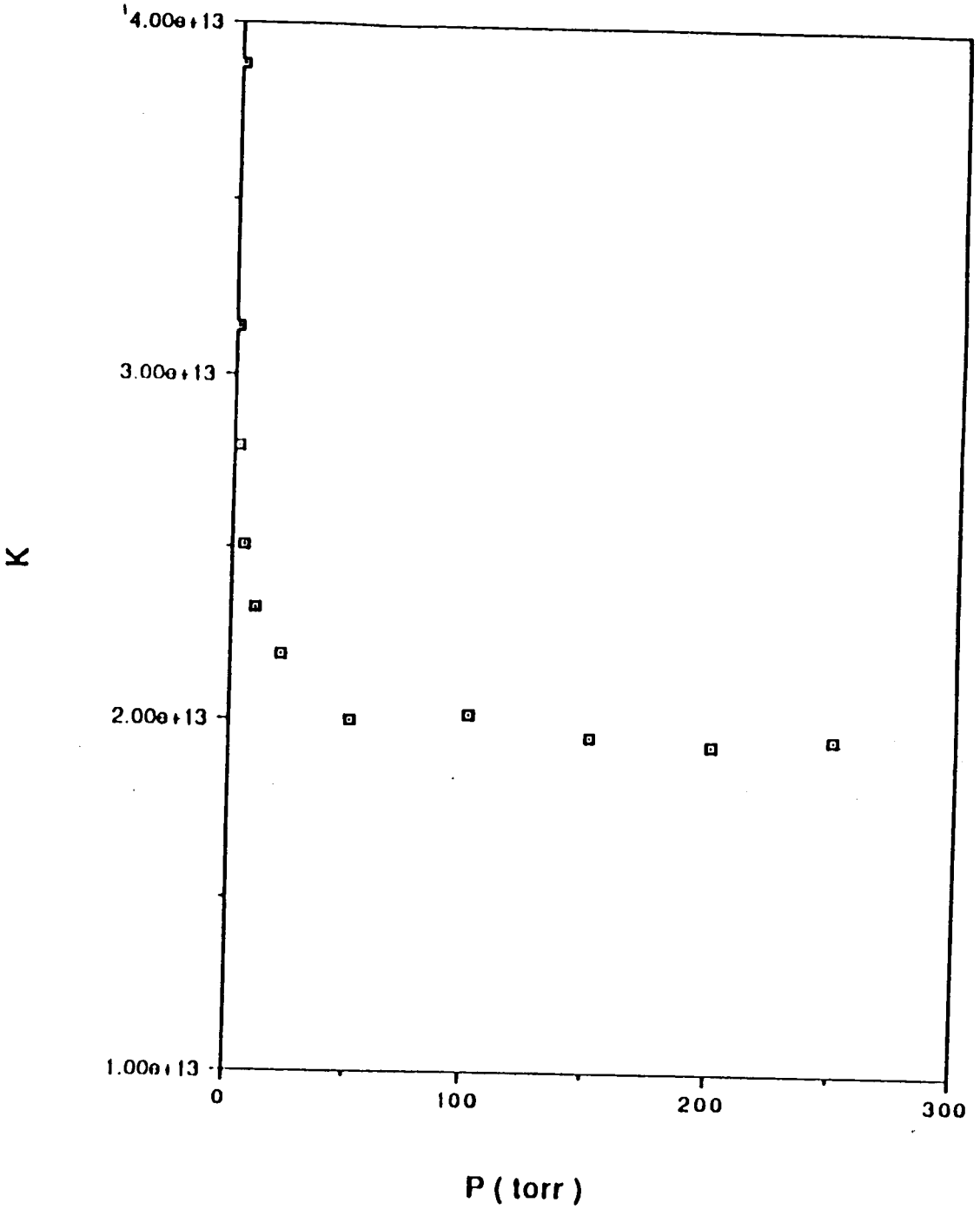

Fig. 6.1 Permeability of oxygen in (111) single crystal silver at 650 °C as a function of upstream pressure

obtained with different high-side pressures of P_0 = 75, 100, 150, 200, and 250 torr. All the permeability data fell on the same straight line as shown in figure 6.2 which agrees with Sievert's law and the assumption that the oxygen atoms move through the silver bulk in the atomic state. The diffusivity data was obtained with P_0 = 150 torr and is shown in figure 6.3. A slight break in linearity occurred in the diffusivity at about 630 °C and appeared to be quite repeatable. The permeability and diffusivity equations determined from the plots are:

$$K_{poly} = 5.8 \times 10^{18} \exp \frac{-22860}{RT} \quad cm^{-1}\text{-}s^{-1} \qquad 6.1$$

$$D_{poly} = 2.96 \times 10^{-3} \exp \frac{-11200}{RT} \quad cm^{2}\text{-}s^{-1} \qquad 630 \leq T \leq 800\ °C \qquad 6.2a$$

$$D_{poly} = 3.997 \times 10^{-2} \exp \frac{-15800}{RT} \quad cm^{2}\text{-}s^{-1} \qquad 400 \leq T \leq 630\ °C \qquad 6.2b$$

(110), (111), (100) single crystal Ag

The permeability data for the (111), (110), and (100) orientations of silver fell almost on the same straight line as is shown in figure 6.4. The equation for the permeability determined from the plot is

$$K = 5.2 \times 10^{18} \exp \frac{-22860}{RT} \quad cm^{-1}\text{-}s^{-1} \qquad 6.3$$

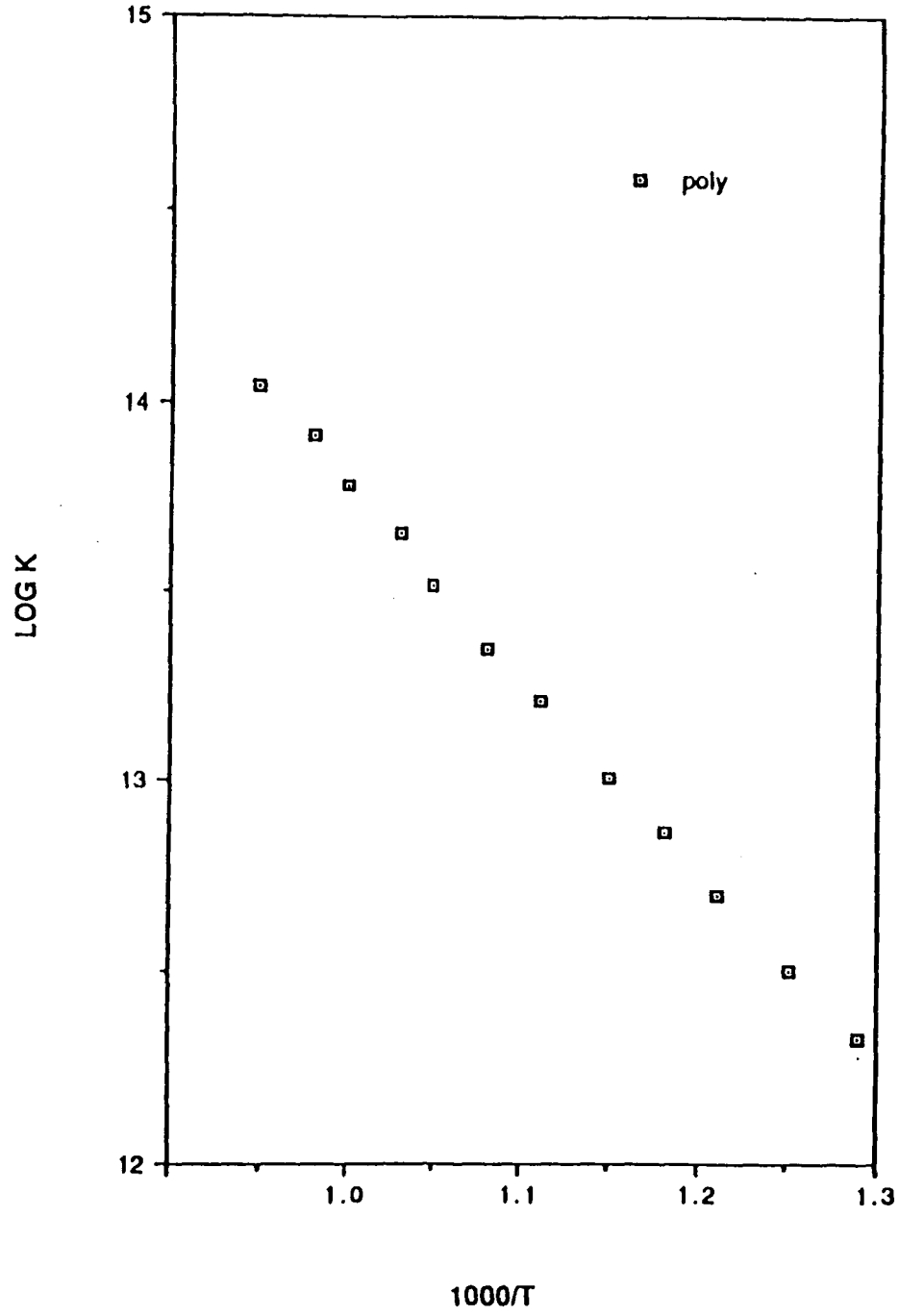

Fig. 6.2 Permeability of oxygen in polycrystalline silver as a function of reciprocal temperature

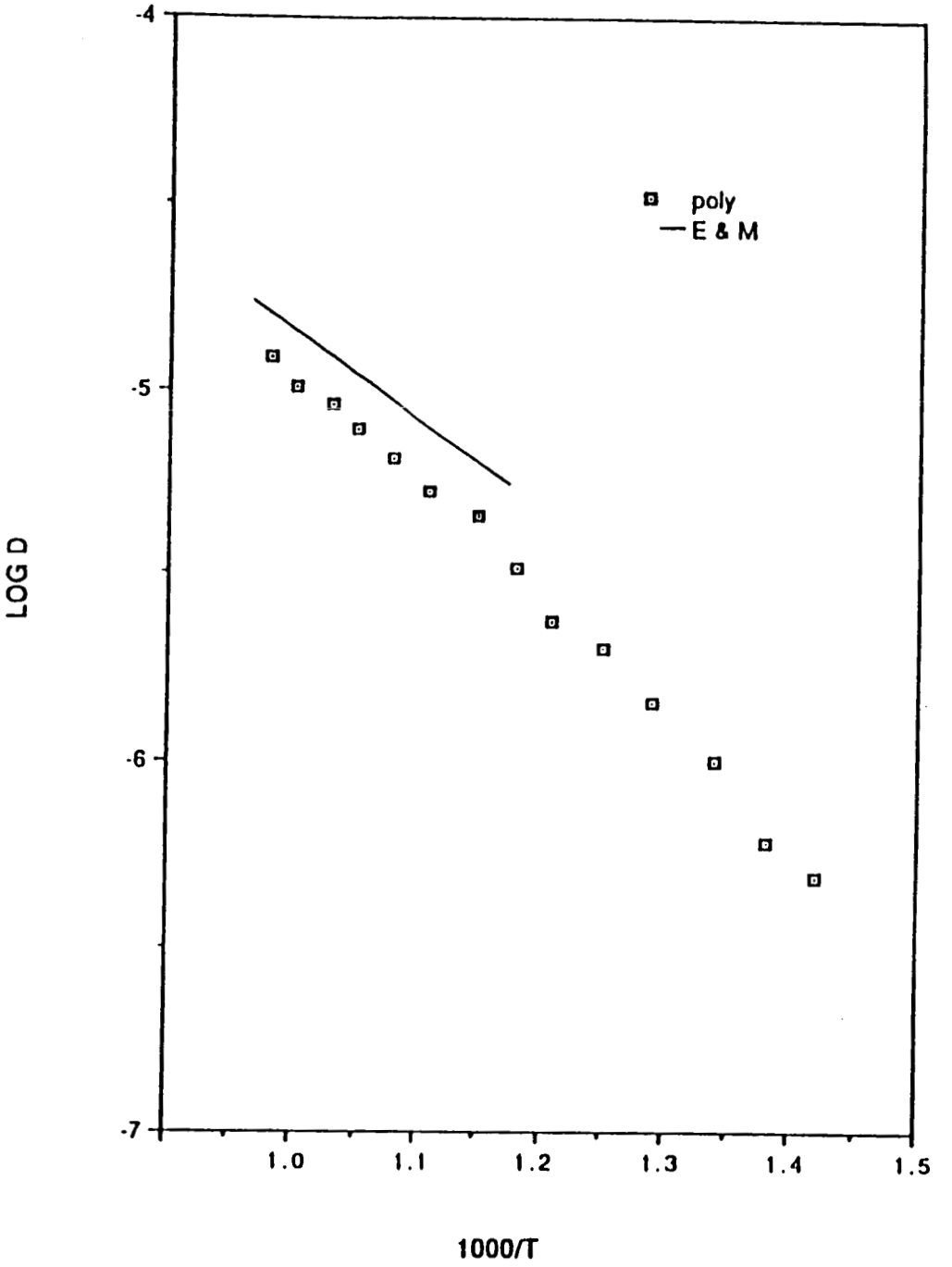

Fig. 6.3 Diffusivity of oxygen in polycrystalline silver as a function of reciprocal temperature

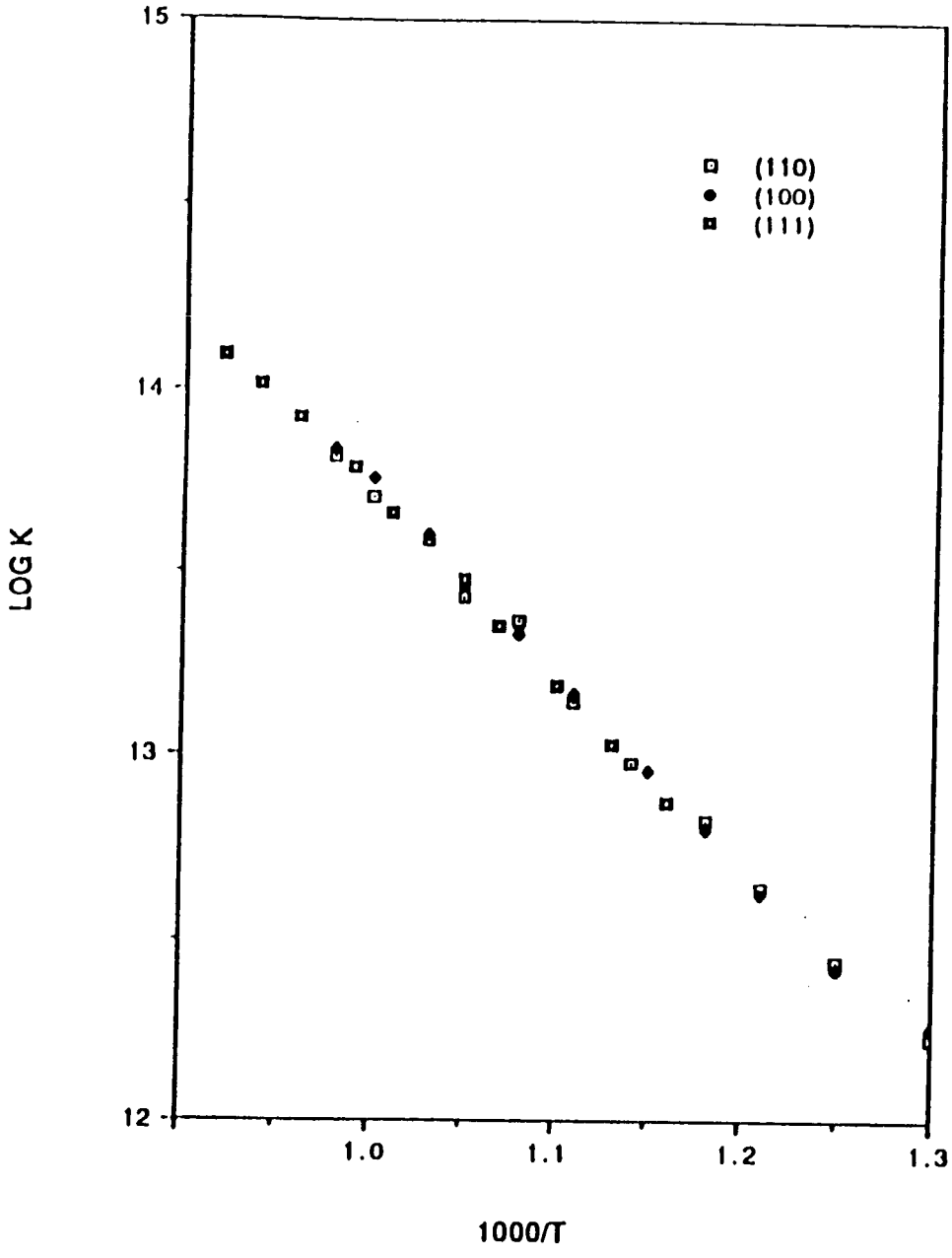

Fig. 6.4 Permeability of oxygen in (111), (110), and (100) single crystal silver as a function of reciprocal temperature

Note here that equation 6.3 is almost identical to that for polycrystalline silver (equation 6.1) except for some slight variation in the preexponential.

The diffusivities, however, for the three crystal orientations are quite different as shown in figure 6.5. The magnitude of diffusivities varies as

$$D_{110} > D_{111} > D_{100}$$

The breaks in linearity of the diffusivity were also observed at about 630 °C for all three single crystals. The diffusivity equations determined from the plot are

$$D_{100} = 9.1 \times 10^{-3} \exp \frac{-14900}{RT} \ cm^2\text{-}s^{-1} \qquad 630 \leq T \leq 800\ °C \qquad 6.4a$$

$$D_{100} = 2.4 \times 10^{-1} \exp \frac{-21000}{RT} \ cm^2\text{-}s^{-1} \qquad 400 \leq T \leq 630\ °C \qquad 6.4b$$

$$D_{111} = 1.0 \times 10^{-2} \exp \frac{-14150}{RT} \ cm^2\text{-}s^{-1} \qquad 630 \leq T \leq 800\ °C \qquad 6.5a$$

$$D_{111} = 1.07 \times 10^{-1} \exp \frac{-18800}{RT} \ cm^2\text{-}s^{-1} \qquad 400 \leq T \leq 630\ °C \qquad 6.5b$$

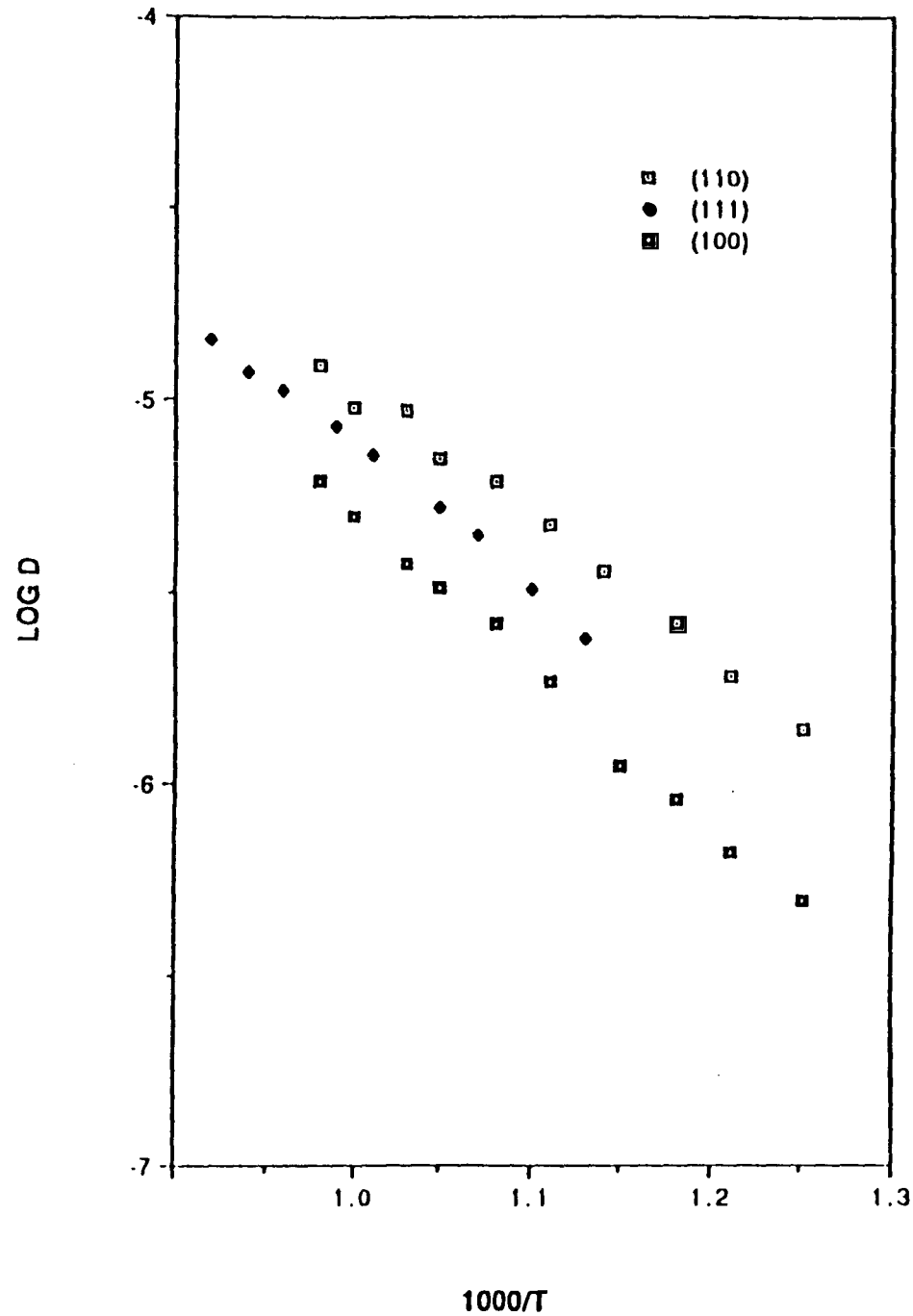

Fig. 6.5 Diffusivity of oxygen in (111), (110), and (100) single crystal silver as a function of reciprocal temperature

$$D_{110} = 1.55 \times 10^{-2} \exp \frac{-14500}{RT} \ cm^2\text{-}s^{-1} \qquad 630 \leq T \leq 800\ °C \qquad 6.6a$$

$$D_{110} = 1.55 \times 10^{-1} \exp \frac{-18500}{RT} \ cm^2\text{-}s^{-1} \qquad 400 \leq T \leq 630\ °C \qquad 6.6b$$

Ag0.05Zr Alloy

The permeability for the Ag0.05Zr alloy fell in a straight line with magnitude higher than the polycrystalline and single crystal silver as shown in figure 6.6. This was the first observed data with a higher K. The diffusivity data for the alloy is shown in figure 6.7. Note that the high temperature data has a slope closer to the low temperature data of the polycrystalline silver. The permeability and diffusivity equations determined from the plots are

$$K_{alloy} = 7.5 \times 10^{18} \exp \frac{-22200}{RT} \ cm^{-1}\text{-}s^{-1} \qquad 6.7$$

$$D_{alloy} = 1.05 \times 10^{-2} \exp \frac{-13200}{RT} \ cm^2\text{-}s^{-1} \qquad 6.8$$

Glow-discharge Studies

Figure 6.8 shows the grow-discharge characteristics. The application of 350 V (dc) and 50 mA for the polycrystalline silver at the upstream pressure of 0.5 torr and membrane temperature of 650 °C rapidly increased the downstream O_2 flux to a factor of approximately of

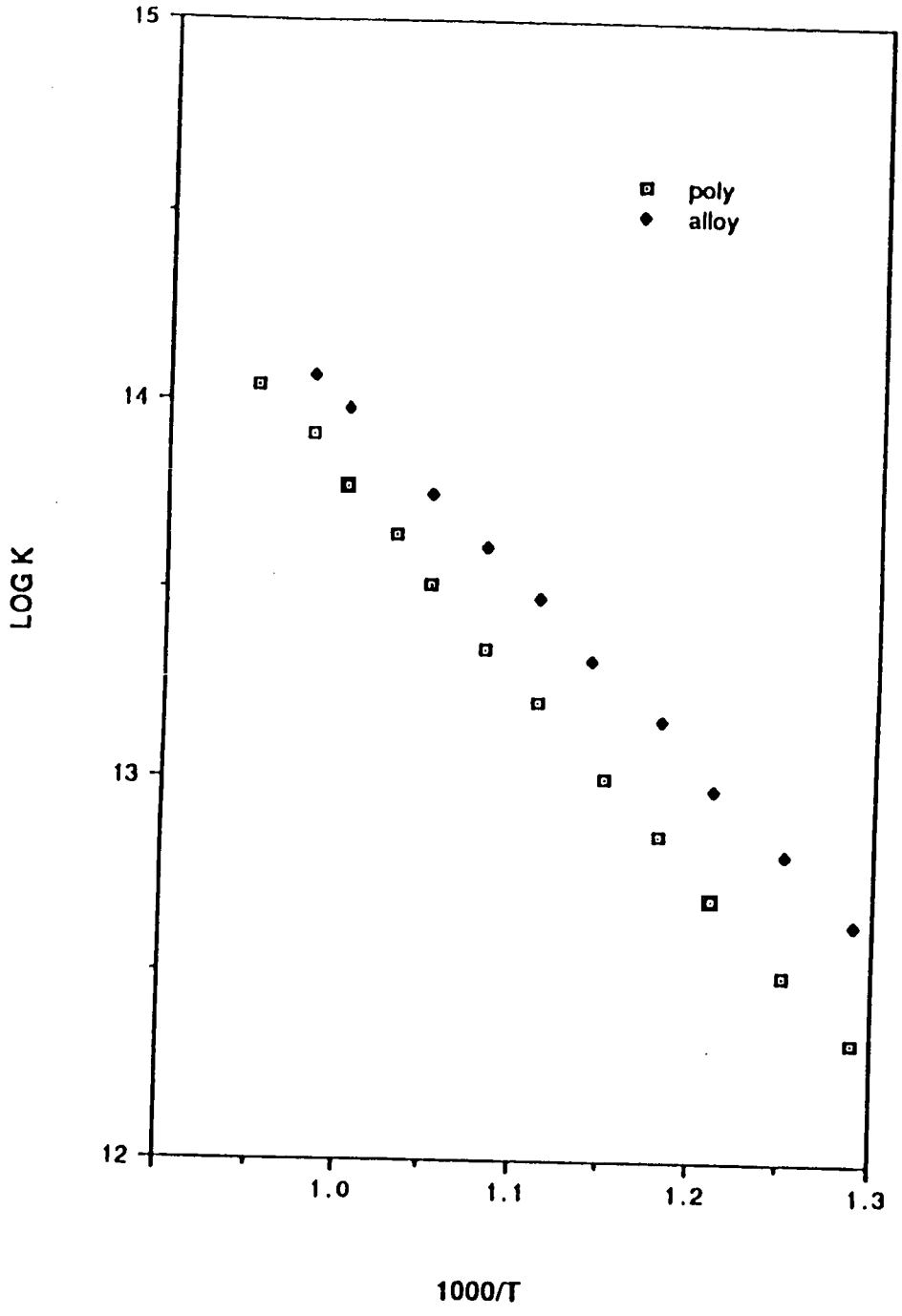

Fig. 6.6 Permeability of oxygen in Ag0.05Zr alloy silver as a function of reciprocal temperature

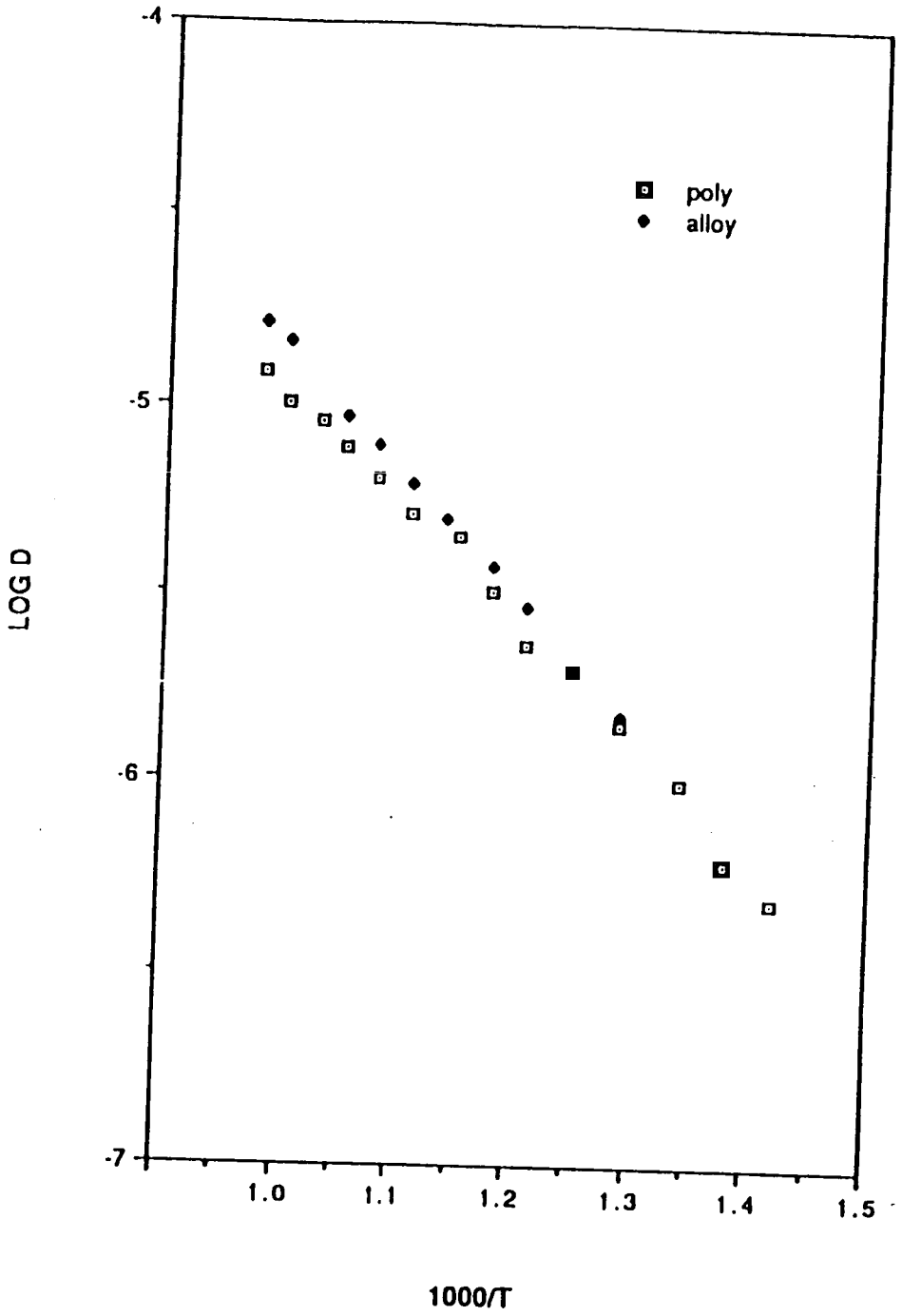

Fig. 6.7 Diffusivity of oxygen in Ag0.05Zr alloy silver as a function of reciprocal temperature

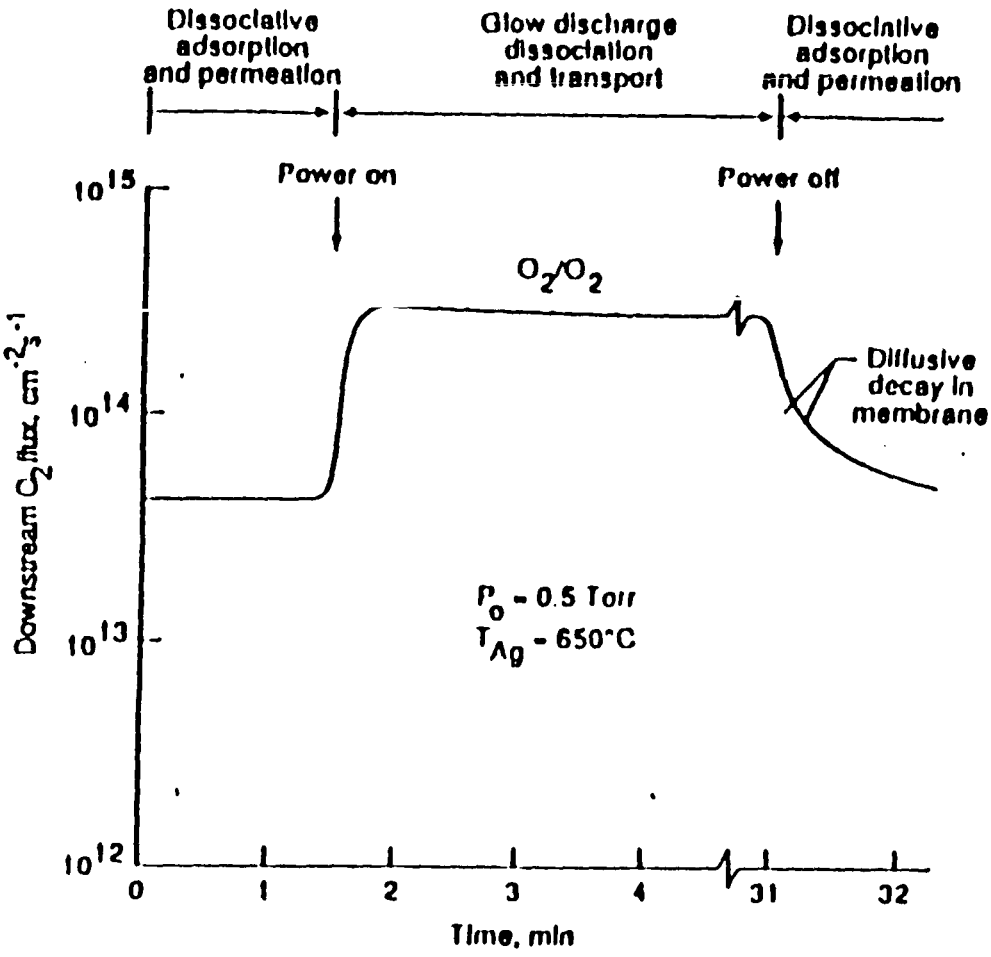

Fig. 6.8 Downstream pressure variations due to oxygen permeation with and without supply side glow-discharge-assisteddissociation.

2.83 X 10^{14} $cm^{-2}s^{-1}$ to that without grow-discharge application. Some slight decay in signal was observed before it reached a steady state, and then when the discharge was quenched, the signal returned to the original steady-state permeation level consistent with thermal dissociative adsorption. This cycle was found to be quite repeatable.

CHAPTER VII

Discussion

The transport of oxygen in silver is unique amongst metals since no other metal will efficiently transport oxygen because of oxidation limitations (except Au which has no stable oxide). Silver forms weak Ag_2O (14 kcal/mole) which clearly is unstable at elevated temperature since the oxygen chemisorbed state is 42 kcal/mole and desorbs at 450 °C. The weak formation energy suggests that there is a very weak chemical interaction between the O and the Ag so that the movement in the lattice from site to site is controlled by physical or electronic constraints (e.g. coulombic repulsion of electron clouds). The radius of the octahedral sites of Ag (r = 0.598 A) compared to the covalent radius of O (r = 0.66 A) has only a difference of about 10%. This is well within the 15 % rule for acceptable strain. This of course suggests that the conditions for transport of oxygen through silver are favorable.

On the other hand, the surface effects restricting the dissociative adsorption of O_2 appear to be quite substantial. Sticking coefficient data is shown as in the table

Temperature	$S_{[110]}$	$S_{[111]}$	$S_{[100]}$
27 °C	3×10^{-3}	1×10^{-5}	1×10^{-5}
217 °C	1×10^{-4}		1×10^{-6}

At the room temperature, The highest sticking coefficients measured for the low index faces is 3 x 10^{-3} for the (110) orientation and it substantially decreases at 217 °C to 1 x 10^{-4}. The (111) and (100) orientations are in the 1 x 10^{-5} to 1 x 10^{-6} range at room temperature and they too substantially decrease at increased temperature. These observations along with the apparently low O (KLL, 503 eV) Auger signal indicate that oxygen molecules make many collisions before one of them is in the right orientation at the right site on the surface when dissociative adsorption occurs. Clearly, this indicates the difficulty in getting atoms on the surface and subsequently dissolved into the bulk. Past researchers have not included sticking coefficient variations as a function of defect density on the low index orientations, so, it is unclear as to whether the higher sticking coefficient on the (110) surface is because of a higher number of defects or because of its crystallographic structure. Low energy electron diffraction (LEED) studies have shown 2 X 1 to 2 X 7 structures (depending on the exposure) where the oxygen atoms lie in the troughs of the rib like structure of the (110) orientation. These LEED results determine the final adsorption sites but say nothing about the dissociative adsorption sites. Clearly, there are many of this problems that require research to uncover the actual mechanism of oxygen transport.

Permeability vs Upstream Pressure (P_0)

Figure 6.1 shows the from 0.5 to 250 torr for the (111) single

crystal silver at a temperature of 650 °C. The value of the permeability is a constant for upstream pressure larger than 50 torr but increases by a factor of 2 from 50 torr down to 0.5 torr. The reason why the permeability goes up below 50 torr is not very clear at this point but it may be related to surface site competition. At low pressures (< 50 torr), the impinging molecules are more efficient in finding sites for dissociative adsorption so a larger fraction are adsorbed and ultimately dissolved. At higher pressures (> 50 torr), these sites are conductance limited that is the permeability is a constant and the overall transport is a function of $P_0^{1/2}$ (Sievert's Law). The permeability and diffusivity data presented here, however, are for pressures 75 torr or greater.

Polycrystalline Ag

The permeability for the large grain polycrystalline silver as shown in figure 6.2 was found to be quite linear and was very repeatable for six separate samples. The activation energy was determined to be 22860 cal/mole and the preexponential was 5.8×10^{18} which is almost identical to the DS product of Eichenauer and Mueller (ref.21). The corresponding flux, J, associated with a $P_0 = 760$ torr at 700 °C for a membrane thickness of 0.0238 cm is 8.26×10^{14} $cm^{-2}s^{-1}$ which represents an indication of the level of pure oxygen which can be inlet into the system.

The diffusivity data for polycrystalline silver (T > 630 °C) shown in figure 6.3 is 0.99 the diffusivity data determined by Eichenauer and

Mueller. The method they employed was the desorption technique which is based on observing the release of gas from a gas-charged metal body in a vacuum after having increased the temperature to some elevated level. Note the scatter in their low pressure data (see fig. 2.2). The experiment presented here was the permeation technique conducted in an ultra-high vacuum environment ($p < 1 \times 10^{-9}$ torr) and the data are very consistent over six runs. Furthermore, the higher impurity silver used in Eichenauer and Mueller's work could also have some surface effect on the magnitude of the diffusivity. Eichenauer and Mueller used 99.99 percent silver melted at an ultimate pressure of ~ 1×10^{-3} torr (which further contaminates the metal) while 99.9999+ percent silver melted at an ultimate pressure of ~ 1×10^{-8} torr was used in this work. Silver is well known to be very sensitive to impurities restricting grain growth, since the segregation of the impurities to the grain boundaries tends to slow down or stop intergranular transfer of silver atoms from smaller to larger grains. Even a modest increase in the impurity level can substantially increase the grain boundary density as well as defects which in turn can provide a higher diffusivity due to the grain boundary and defect diffusion component. Unfortunately, no microstructural studies were performed in their work to make a direct comparison.

The value of the activation energy (E_a = 11200 cal/mole) found in this work is almost the same as obtained by Eichenauer and Mueller (E_a = 11000 cal/mole) in the temperature above 630 °C, as can be seen from the figure 6.2. The first few runs over the temperature range produced

overall linear diffusivity plots, but subsequent data began to reveal a slight break in linearity at about 630 °C. The value of the activation energy (E_a = 15800 cal/mole) below 630 °C is much higher than above 630 °C. This is probably because of the higher efficiency of traps at low temperatures caused by grain boundaries, dislocations, twins, inclusions, and pores. In the work of Eichenauer and Mueller, one can question what actually occurs below 600 °C because of lack of oxygen purging and also because of less pure conditions. Furthermore, the scatter is so severe that a linearity break could not be detected. Mitchell et al. (ref.27) have shown the effects of hydrogen trapping in copper due to the addition of substitutional impurities Er, Zr, and Ti. As observed in this work, they noted no change in the linearity of the permeability, even up to 4 atomic percent of Zr, but they did observe a significant decrease in the magnitude of the effective diffusivity (D_{eff} represents the effect of the trap in contrast to the D in pure Cu). Further, the slope of the D_{eff} (for all impurities) in an Arrhenius plot was also greater than for the D in the pure Cu and represents an increased activation energy because of the trap. Although we are concerned with interstitials and with far less of an impurity concentration, it is quite likely that only crystallographic defects could serve as traps and be active in this work to give rise to the relatively smaller break.

(110), (111), (100) Ag

No data in the literature could be found for oxygen permeation

through single crystals of silver or for any other gas through a metal. Although the compression of metal to metal sealing between two small stainless steel flanges (mini) caused some recrystallization around the periphery of the silver membranes (~ 25% of total area) during the high temperature excursions, the center section of the samples remained a complete single crystal. As shown in figure 6.4, the permeabilities of the(111), (110), and (100) orientations all fell along a linear Arrhenius plot suggesting that the overall transport was the same. The activation energy was 22860 cal/mole and the preexponential was 5.2×10^{18} which is also very near to that found for the polycrystalline silver. This similarity must indicate that the transport limitation is the same for single crystal and polycrystalline samples. The polycrystalline sample, however, was very large grain and since it is just an aggregation of different orientations and no variation in K was observed for the three orientations studied, this appears to be consistent behavior. In other words, whatever is responsible, the limitation must be common to polycrystalline and single crystal material. The activation energy for diffusion of oxygen through the three single crystals are all similar which is between 14150 to 14900 cal/mole in the temperature range above 630 °C and 18500 to 21000 cal/mole in the temperature range below 630 °C. This is considerably larger than the activation energy of the polycrystalline silver (11200 cal/mole in the temperature range above 630 °C and 15800 cal/mole in the temperature range below 630 °C). The overall activation energy is the sum of the activation energy of the lattice diffusion, defect diffusion, grain boundary diffusion, and surface

diffusion, but it is unclear as to which component is different in the single crystal and polycrystalline materials. The activation energy represents the energy barrier between octahedral sites and certainly should be the same for any orientation. The only difference in the polycrystalline is maybe a grain boundary or defect density component that could lessen the E_a magnitude.

In contrast to the same permeability, the magnitude of the diffusivity is not the same for the three different crystal orientations. Since the oxygen resides primarily in the octahedral sites of the lattice (constant per unit volume), the solubility, S, of the different orientations should be the same. The permeability K = DS then should vary with D. Since K is a constant, there is a problem with either the K = DS assumption or there is a possible upstream surface limitation. Consider the surface limitation possibility, the relation of K = DS could be modified to

$$K = DS [1 - f(s)]$$

where $f(s) \leq 1$ is some function of surface limitation. The f(s) could be some function of the sticking coefficient or surface defects or some other surface factors. When f(s) = 0, K = DS. When f(s) = 1, then the surface is completely impenetrable and K = 0. The fact that the permeability data is linear requires that the functional form should be computable with an Arrhenius plot i.e.

C-2

$$\ln K = \ln D + \ln S + \ln [\, 1 - f(s) \,]$$

There is, however, no available research that provides insight into the functional form of f(s) such as the variation in defect density with crystal orientation and the variation in sticking coefficient at elevated temperatures (400 - 800 °C). Since the sticking coefficient has been shown to substantially decrease with temperature, it may be very small above 400 °C and no longer a significant function at crystalline orientation. In this temperature range, perhaps all surfaces have similar adsorption properties. This is clearly a speculation, however.

The diffusivity variation between the single crystals can also be examined in a fundamental way. Figure 7.1 shows the FCC unit cell with indicated octahedral sites. Also shown on this figure are the directions of the single crystal orientations. At a given temperature, the atomic jump probability from one octahedral site to another must be the same, and this is reflected in the similar activations energies of diffusion for the three orientations. This implies that for a given interval, Δt, the number of jumps, N, must be the same, so the question arises as to what is the mean distance traveled by an oxygen atom when the permeation membrane is oriented in the three directions shown in figure 7.1. Clearly, in the [110] direction, the atoms can move along a straight line in the oriented direction so that diffusion through can proceed rapidly. All jumps are in the <110> family. In the [100] direction, at least two jumps are required to have a [100] displacement. And in the [111] at least three jumps are

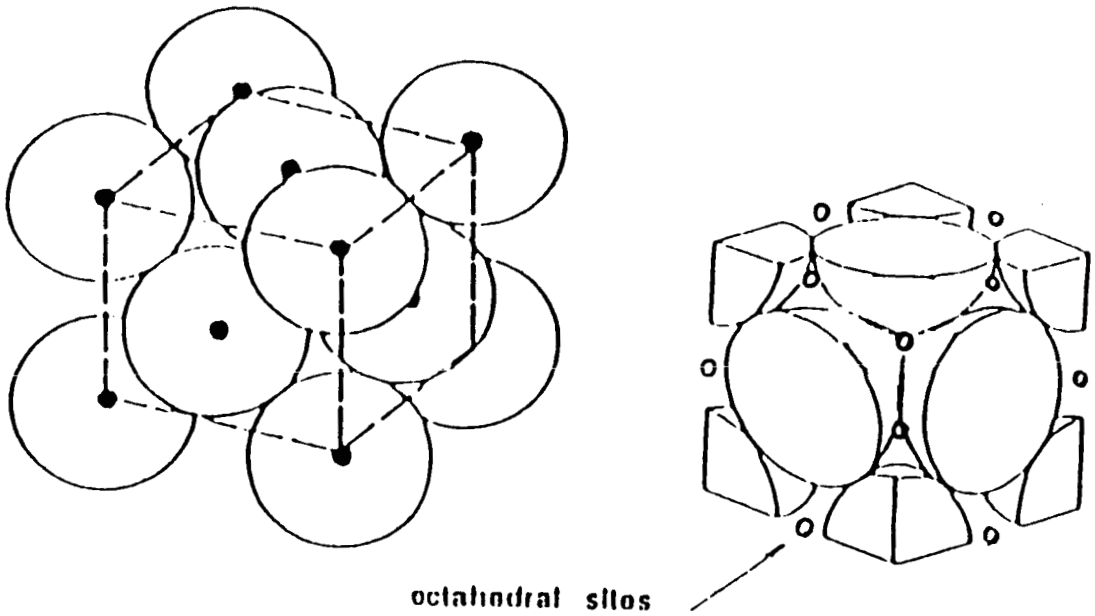

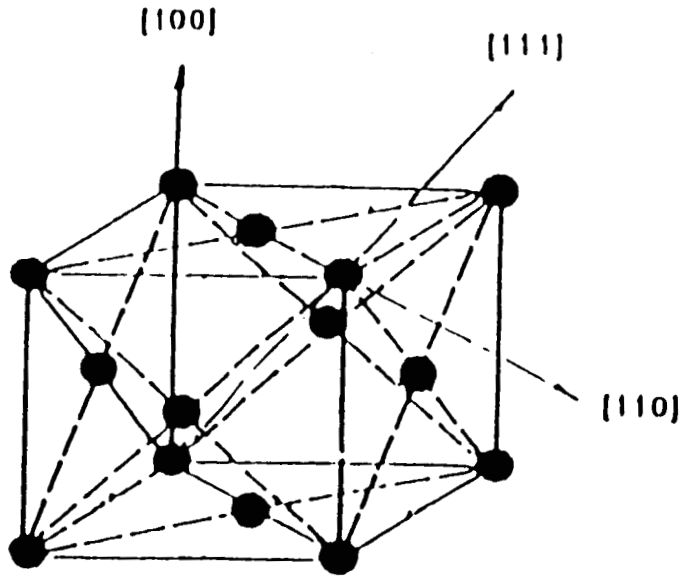

Fig. 7.1 Schematic view of face-centered cubic cell with O on octahedral sites

required for a [111] displacement but the net displacements are all different. It can be calculated that for the same number of jumps, the maximum possible displacement in three different direction are different. Therefore

$$L_{[110]} > L_{[111]} > L_{[100]}$$

and

$$L^2_{[110]} > L^2_{[111]} > L^2_{[100]}$$

Compare with the well-known relation

$$D = \frac{\langle x^2 \rangle}{2t}$$

where $< x^2 >$ is the mean spuare displacement and t is the interval of time. This suggests that

$$D_{[110]} > D_{[111]} > D_{[100]}$$

Further

$$\frac{D_{[111]}}{D_{[110]}} = \frac{2}{3}; \qquad \frac{D_{[100]}}{D_{[110]}} = \frac{1}{2}; \qquad \frac{D_{[100]}}{D_{[111]}} = \frac{3}{4};$$

The experimental data at T = 700 °C are

$$\frac{D_{[111]}}{D_{[110]}} = 0.57 ; \qquad \frac{D_{[100]}}{D_{[110]}} = 0.41 ; \qquad \frac{D_{[100]}}{D_{[111]}} = 0.72 ;$$

This is reasonable agreement within the error observed from recrystallinzation (i.e. < 25%).

Ag0.05Zr Alloy

The addition of 0.05 wt percent Zr to the Ag was to provide some substantial grain refinement and defects in the Ag in order to enhance the transport by grain boundary and/or defect diffusion. Figure 6.6 show the first increase in the overall permeability that was observed in this research. The permeability for Ag0.05Zr alloy silver fell along a straight line which is a factor of 1.86 higher than the polycrystalline silver as shown in figure 6.6. Figure 7.2 shows the microstructure (before the experiment) of this alloy. It is clear that the 0.05 percent Zr gives a much higher grain boundary and defect density compared to the polycrystalline silver or single crystal silver. This provides more reservoirs for oxygen which will increase the solubility and diffusivity to give the higher permeability. Furthermore, the sticking coefficient is probably larger for the alloy compared to the pure silver because the chemical affinity of Zr to oxygen is much larger and there are many more surface defects for dissociative adsorption of O_2. Thus, there may be more of a surface effect in this alloy compared to single crystalline and polycrystalline silver.

Fig. 7.2 Microstructure of the Ag0.05Zr membrane

This latter effect may actually be the controlling step in the mechanism.

The diffusivity data for Ag0.05Zr also fell on a straight line very close to that of polycrystalline silver. The activation energy at the temperature above 630 °C (13200 cal/mole) is a little larger than for the polycrystalline silver (11200 cal/mole). Since the chemical reactivity of the Zr to oxygen is much higher than the silver to oxygen, oxygen atoms could be trapped in the alloy lattice, especially at the lower temperatures. The overall activation energy is equal to the trapping energy plus the internal energy which suggest that because of this greater trapping energy, the break at 630 °C has almost disappeared. Because this is such a dilute alloy, the activation energy is not substantially greater than the Ag. It is still unclear however whether the increased surface effect or the higher density of oxygen reservoirs created the higher permeability.

Glow Discharge Studies

The effect of the surface on the transport was further examined by using a glow discharge on the upstream side to enhance the formation of oxygen atoms. As shown in figure 6.8 the flux of oxygen substantially increased from the steady state dissociative adsorption level (p = 0.5 torr O_2) by a factor of 6. This indicates that there is a definite surface limitation for normal dissociative adsorption. Higher pressures could not be employed because of mean free path problems. The application of 350 V(dc) and 50 mA rapidly increased the downstream O_2 flux to a factor of

approximately 2.83 x 10^{14} $cm^{-2}s^{-1}$. Presumably, at low values of E/n, where E is the electric field and n is the molecular number density (< 10^{-15} V cm^2), the electron impact dissociation in the glow discharge can be represented by

$$O_2 + e \rightarrow O + O + e$$

or

$$O_2 + e \rightarrow O + O^* + e$$

which are the $A(^3\Sigma_u^+)$ and the $B(^3\Sigma_u^-)$ states, respectively (ref.31 and ref.32). In this work, the E/n value is on the order of 10^{-14} V cm^2, thus possibly producing a substantial quantity of ions and excited states in addition to the neutral species. The oxygen neutral positive ion species formed in the vicinity of the membrane (cathode fall region) first adsorb on the Ag surface, then dissolve into the bulk, and then diffuse to the downstream membrane face where they associate with another oxygen atom and thermally desorb as O_2. The increased signal during the glow discharge suggests that the adsorption and dissolution rate for oxygen atoms is substantially greater than for the previously conducted permeation experiments where O_2 molecules are dissociatively adsorbed.

dislocations, twins, inclusions and pores. The diffusivity equations obtained are

$$D_{poly} = 2.96 \times 10^{-3} \exp \frac{-11200}{RT} \ cm^2\text{-}s^{-1} \qquad 630 \leq T \leq 800\ °C$$

$$D_{poly} = 3.997 \times 10^{-2} \exp \frac{-15800}{RT} \ cm^2\text{-}s^{-1} \qquad 400 \leq T \leq 630\ °C$$

4. The permeabilities of the (110), (111) and (100) single crystal silvers all fell along a linear Arrhenius plot which suggest that the overall transport was the same. The activation energy and the preexponential are very similar to that found for the polycrystalline silver which indicates that the transport limitation is probably the same, even though there is some substantial difference in the microstructure. The permeability equation for the single crystals silver is

$$K = 5.2 \times 10^{18} \exp \frac{-22860}{RT} \ cm^{-1}\text{-}s^{-1}$$

5. The magnitude of the diffusivity was found to be different for the three different crystal orientations. Since the solubility, S, should be the same for different orientations, this does not obey the relation K = DS. There is a problem with either variation of the mathematical formalism or there is a limitation at the upstream surface. The diffusivity equations of the three single crystals are

$$D_{100} = 9.1 \times 10^{-3} \exp \frac{-14900}{RT} \ cm^2\text{-}s^{-1} \qquad 630 \leq T \leq 800\ °C$$

$$D_{100} = 2.4 \times 10^{-1} \exp \frac{-21000}{RT} \quad cm^2\text{-}s^{-1} \qquad 400 \leq T \leq 630\ °C$$

$$D_{111} = 1.0 \times 10^{-2} \exp \frac{-14150}{RT} \quad cm^2\text{-}s^{-1} \qquad 630 \leq T \leq 800\ °C$$

$$D_{111} = 1.07 \times 10^{-1} \exp \frac{-18800}{RT} \quad cm^2\text{-}s^{-1} \qquad 400 \leq T \leq 630\ °C$$

$$D_{110} = 1.55 \times 10^{-2} \exp \frac{-14500}{RT} \quad cm^2\text{-}s^{-1} \qquad 630 \leq T \leq 800\ °C$$

$$D_{110} = 1.55 \times 10^{-1} \exp \frac{-18500}{RT} \quad cm^2\text{-}s^{-1} \qquad 400 \leq T \leq 630\ °C$$

6. The magnitude of the diffusivity variation was examined by considering the different lattice orientations and was found that the experimental data is in general agree with theoretical estimates.

7. The permeability for Ag0.05Zr alloy is a factor of 1.86 higher than polycrystalline silver. The 0.05 percent Zr gives a much higher grain boundary and defect density to provide more reservoirs for oxygen which will increase the solubility and give the higher permeability. The diffusivity data is very close to the polycrystalline silver and the break at 630 °C has almost disappeared. Since the chemical activity of the Zr to oxygen is much higher than the silver to oxygen, the oxygen atoms could be trapped in the alloy lattice even at the high temperature (above 630 °C). It may also substantially increase the defects where dissociative adsorption occurs. The diffusivity equation for the alloy is

$$D_{alloy} = 1.05 \times 10^{-2} \exp \frac{-13200}{RT} \ cm^2\text{-}s^{-1}$$

8. The effect of the surface limitation on transport was further examined by using a glow discharge on the upstream side to enhance the formation of oxygen atoms. It was found that the flux of oxygen substantially increased from the steady state dissociative adsorption level by a factor of 6. This indicates that there is a definite surface limitation for normal dissociative adsorption. The increased signal during the glow discharge suggests that the adsorption and dissolution rate for oxygen atoms is substantially greater than for the previously conducted permeation experiments where O_2 molecules are dissociatively adsorbed. A theoretical estimate suggests that there are conditions where surface limitation of the transport can occur. It appears to be a function of the amount of atomic oxygen formation.

References

1. Engelhardt, H.A.; and Menzel, D.: Adsorption of Oxygen on silver Single Crystal surfaces. Surf. Sci., vol. 57, no. 2, July 1976, pp. 591 - 618.

2. Barteau, M.A.; and Madix, R.J.: The adsorption of Molecular Oxygen Species on Silver (110). Surf. Sci., vol. 97, no. 1, 1980, pp. 101 - 110.

3. Backx, C.; De Groot, C.P.M.; and Biloen, P.: Adsorption of Oxygen on Ag(110) Studied by High Resolution ELS and TPD. Surf. Sci., vol. 104, no. 1, Mar. 1981, pp. 300 - 317.

4. Grant, R.B.; and Lambert, R.M.: Basic Studies of the Oxygen Surface Chemistry of Silver: Chemisorbed Atomic and Molecular Species on Pure Ag(111). Surf. Sci., vol. 146, no. 1, Oct. 1981, pp. 256 - 268.

5. Campbell, Charles T.: Atomic and Molecular Oxygen Adsorption on Ag(111). Surf. Sci., vol. 157, no. 1, July 1985, pp. 43 - 60.

6. Puschmann, A.; and Haase, J.: Surface EXAFS of the (2 X 1) Oxygen Adlayer on Ag(110). Surf. Sci., vol. 144, nos. 2/3, Sept. 1984, pp. 559 - 566.

7. Eickmans, J.; and Otto, A.: The Transition From Physisorbed to Chemisorbed Oxygen on Silver Films Studied by Photoemission. Surf. Sci., vol. 149, no. 1, Jan. 1985, pp. 293 - 312.

8. Peuckert, M.: On the Adsorption of Oxygen and Potassium Hydroxide on Silver. Surf. Sci., vol. 146, nos. 2/3, Nov. 1984, pp. 329 - 340.

9. Bange, K.; Madey, T.E.; and Sass, J.K.: Characterization of OH(ad) Formation by Reaction Between H_2O and O(ad) on Ag(110). Surf. Sci., vol. 152/153, pt. 1, Apr. 1985, pp. 550 - 558.

10. Prince, K.C.; and Bradshaw, A.M.: Valence Level Photoelectron Spectroscopy of the Oxygen and Carbonate Species on Silver (110). Surf. Sci., vol. 126, nos. 1 - 3, Mar. 1983, pp. 49 - 57.

11. Au, Chak-Tong; Singh-Boparai, Sunder; Roberts, M.Wyn; and Joyner, Richard W.: Chemisorption of Oxygen at Ag(110) Surfaces and Its Role in Adsorbate Activation. J. Chem. Soc., Faraday Trans. 1, Vol. 79, 1983, pp. 1779 - 1791.

12. Sporken, R.; Thiry, P.A.; Pireaux, J.J.; Caudano, R.; and Adnot, A.: Work Function Measurements with a High Resolution Electron Energy Loss Spectrometer: Application to the Interaction of Oxygen with Ag(110). Surf. Sci., vol. 160, no. 2, Sept. 1985, pp. 443 - 450.

13. Rovida, G.; Pratesi, F.; Maglietta, M.; and Ferroni, E.: Effects of Oxygen on Silver Surface Structure. J. Vac. Sci. & Technol., vol. 9, no. 2, Mar./Apr. 1972, pp. 796 - 799.

14. Prince, K.C.; Paolucci, G.; Bradshaw, A.M.; Horn, K.; and Mariani, C.: Oxygen Adsorption on Ag(110): Observation of a Precursor State. Vacuum, vol. 33, nos. 10 - 12, Oct. - Dec. 1983, p. 867.

15. Kagawa, S.; Iwamoto, M.; Morita, S.; and Seiyama, T.: Isotopic Study of the Temperature- Programmed Desorption of Oxygen From Silver. J. Chem. Soc., Faraday Trans. 1, vol. 78, 1982, pp. 143 - 146.

16. Rovida, G.; and Pratesi, F.: Chemisorption of Oxygen on the Silver (110) Surface. Surf. Sci., vol. 52, no. 3, Nov. 1975, pp. 542 - 555.

17. Goddard, P.J.; and Lambert, R.M.: Basic Studies of the Oxygen Surface Chemistry of Silver: Oxygen Dioxygen, Oxide and Superoxide on Rubidium- Dosed Ag(111). Surf. Sci., vol. 107, nos. 2/3, June 1981, pp. 519 - 532.

18. Heiland, W.; Iberl, F.; Taglauer, E.; and Menzel, D.: Oxygen Adsorption on (110) Silver. Surf. Sci., vol. 53, Dec. 1975, pp. 383 - 392.

19. Zanazzi, E.; Maglietta, M.; Bardi, U.; Jona, F.; and Marcus, P.M.: Test of Structural Models for Ag(110) 1 X 2-0 by LEED Intensity Analysis. J.

Vac. Sci. & Technol., vol. 1, no. 1, Jan. - Mar. 1983, pp. 7 - 11.

20. Joyner, R.W.; and Roberts, M.W.: A Study of the Adsorption of Oxygen on Silver at High Pressure by Electron Spectroscopy. Chem. Phys. Lett., vol. 60, no. 3, Jan. 15, 1979, pp. 459 - 462.

21. Eichenauer, Walter; and Jueller, Gudrun: Diffusion and Solubility of Oxygen in Silver. Zeitschrift fuer Metallkunde, Bd. 53, 1962, pp. 321 - 324.

22. Coles, R.E.: The Permeability of Silver to Oxygen. British J. Appl. Phys., vol. 14, 1963, pp. 342 - 344.

23. Beavis, L.C.: Oxygen Permeation Through Silver. Rev. Sci. Instrum., vol. 43, no. 1, Jan. 1972, pp. 122 - 127.

24. Ramanarayanan, T.A.; and Rapp, R.A.: The Diffusivity and Solubility of Oxygen in Solid Nickel. Metall. Trans., vol. 3, no. 12, Dec. 1972, pp. 3239 - 3246.

25. Gryaznov, V.M.; Gul'yanova, S.G.; and Kanizius, S.: Diffusion of Oxygen Through a Silver Membrane, Russian J. Phys. Chem., vol. 47, no. 10, 1973, pp. 1517 - 1518.

26. Outlaw, R.A; Sankaran, S.N.; Hoflund, G.B; and Davidson, M.R.: Oxygen

Transport Through High-purity, Large-grain Ag. J. mater. Res. 3(6), Nov/Dec 1988, pp. 1378 - 1384.

27. Mitchell, D.J.; Harris, J.M.; Patrick, R.C.; Boespflug, I.P.; and Beavis, L.C.: Deuterium Permeation Through Copper With Trapping Impurities. J. Appl. Phys., vol. 53, no. 2, Feb. 1982, pp. 970 - 978.

28. Perkins, W.G.: Permeation and Outgassing of Vacuum Materials. J. Vac. Sci. & Tehcnol., vol. 10, no. 4, July/Aug. 1973, pp. 543 - 556.

29. Crank, J.: Mathematics of Diffusion (Oxford U. P., Oxford, 1967), 2nd ed., pp.

30. Paul, W.; Reinhard, H. P.; and Von Zahn, U.: Das Elektrische Massenfilter als Massenspektrometer und Isotopentrenner. Z. Phys., Bd. 152, Heft 2, 1958, pp. 143 - 182

31. Corvin, K.K. and Corrigan, S.J.B.: J. Chem. Phys. 50. 2570 (1969)

32. Barton, M.J. and Von Engel, A.: Phys. Lett. A32, 173 (1970)

CHAPTER VIII

Conclusions

The studies of permeation of oxygen through large grain polycrystalline silver, through the (110), (111) and (100) single crystals of silver and through Ag0.05Zr alloy have been made. The following are the conclusions obtained from this experiment:

1. The permeability is a constant for the upstream pressure above 50 torr and overall transport is a function of $P_0^{1/2}$ (Sievert's Law). The reason why the value of the permeability increased by a factor of 2 from 50 to 0.5 torr is not very clear but it may be related to the surface site competition.

2. The permeability for the large grain silver was found very repeatable and quite linear in the Arrhenius plot over the temperature range 400 - 800 °C. The permeability equation obtained is

$$K_{poly} = 5.8 \times 10^{18} \exp \frac{-22860}{RT} \quad cm^{-1}\text{-}s^{-1}$$

3. A slight break in linearity of the diffusivity at about 630 °C was observed for the large grain silver. The value of the activation energy above 630 °C is almost the same as obtained by others studying O/Ag system but is higher below 630 °C. This is probably because of the higher efficiency of traps at low temperatures caused by grain boundaries,